# Active Microrheology of Mammalian Cells to Elucidate the Mechanical Relaxation of Alpha-actinin

Christopher Sitaras, Biological and Biomedical Engineering

McGill University, Montreal, December 2018

A thesis submitted to McGill University in partial fulfillment of the requirements of the degree of Master of Engineering

## Abstract

The actin cytoskeleton is a key determinant of cell force production, mechanical integrity and structure, and mechanosensation. An essential yet often overlooked element of the actin cytoskeleton is the crosslinker, alpha-actinin 4 (ACTN4), which *in vitro*, has been shown to exhibit catch-bond behavior and determine the mechanical relaxation of purified actin networks. ACTN4's role in determining the mechanical properties of the cytoplasm, however, is unclear. Here we use a combination of Passive Microrheology (PMR), Optical Magnetic Twisting Cytometry (OMTC), and Magnetic Tweezers (MTs) to probe the moduli and creep behavior of the cytoplasm in living cells. We use cell-surface adhered of 4.66 μm ferrimagnetic iron oxide particles or 200 nm fluorescent super-paramagnetic particles as probes, and then measure their displacement due to a force regime. The quantified time-dependent displacement of the particles is applied to mathematical models in order to ascertain the viscoelastic properties of the cytoplasm. To evaluate the role of ACTN4, we employ two cell lines: wild type ACTN4, and a mutated variant (K255E), which has previously been shown to exhibit stronger actin binding and has been implicated in kidney pathology. These results present some of the first cytoplasmic creep measurements related to crosslinker binding kinetics and provide insight into the detailed cytoskeleton relaxation responsible for cell mechanics.

## Résumé

Le cytosquelette d'actine est un component important dans la production de force cellulaire, de l'intégrité et de la structure mécaniques, et de la mécanosensation. Un élément essentiel, mais souvent négligé, du cytosquelette d'actine est l'agent de réticulation, l'alpha-actinine 4 (ACTN4), qui s'est révélé *in vitro* présenter un comportement de capture et de déterminer la relaxation mécanique des réseaux d'actine purifiés. Le rôle de ACTN4 dans la détermination des propriétés mécaniques du cytoplasme n'est toutefois pas clair. Ici, nous utilisons une combinaison de microrhéologie passive (OMR), de cytométrie de torsion magnétique optique (OMTC) et de pinces magnétiques (MT) pour sonder le comportement des modules et du fluage du cytoplasme dans des cellules vivantes. Nous utilisons comme sonde des particules d'oxyde de fer ferrimagnétique de 4,66 µm ou des particules super-paramagnétiques fluorescentes de 200 nm adhérant à la surface d'une cellule, puis mesurons leur déplacement dû à un régime de force. Le déplacement quantifié dépendant du temps des particules est appliqué à des modèles mathématiques afin de déterminer les propriétés viscoélastiques du cytoplasme. Pour évaluer le rôle de ACTN4, nous utilisons deux lignées cellulaires: ACTN4 de type sauvage et un variant muté (K255E), dont il a déjà été démontré qu'ils présentaient une liaison plus forte à l'actine et qui étaient impliqués dans la pathologie du rein. Ces résultats présentent certaines des premières mesures de fluage cytoplasmique liées à la cinétique de liaison à l'agent de réticulation et permettent de mieux comprendre la relaxation détaillée du cytosquelette responsable de la mécanique cellulaire.

# Table of Contents

## List of Figures

## Acknowledgements

I would like to thank my supervisor, Professor Allen Ehrlicher, for financial, academic, research, and emotional support throughout my Master's degree. Without his encouragement and perseverance, I could not have achieved this milestone.

A special thanks to Professor J. Matt Kinsella, who's valued input during the project assisted my progression.

A heartfelt thanks to all the collaborators and colleagues that assisted my research in varying capacities: Professor Stephen Michnick Lab, Adele Khavari, Ali Amini, Haruka Yoshie, Ajinkya Gharge, Luv Srivastava, and Johanan Idicula.

Lastly, I would like to thank funding agencies, NSERC, FRQNT, and CCS for allowing me to develop this project.

## Contribution of Authors

For this research, Christopher Sitaras performed all the research, including review of literatures, design and build of devices, design and conduction of experiments, and data analysis. Christopher Sitaras is the only author of this thesis. Professor Allen Ehrlicher provided valuable guidance for research goals and methods, as well as review of this thesis.

# 1. Introduction

The cell is an exceptionally complex assembly of matter; understanding how it comes together to provide the structural framework allowing life to exist is essential to a basic understanding of life itself. The cell's structural framework is understood to be viscoelastic, and that the cell can be fluidized or stiffened depending on activity [1]. Cells exhibit varied viscoelastic properties due to the active network of motor proteins in their cytoskeletal network and can change their properties on time scales of seconds to minutes [2]. Several methodologies have been developed for use in understanding the mechanics of the cells, such as, Optical Tweezers (OTs), Traction Form Microscopy (TFM), Passive Microrheology (PMR), Atomic Force Microscopy (AFM), Optical magnetic twisting cytometry (OMTC), Magnetic Tweezers (MTs) and Force Spectrum Microscopy (FSM) [3] [4] [5] [6]. Among these methodologies, the OTs, PMR, OMTC, and MTs have the spatiotemporal resolution to probe the mechanics inside the cell.

Cell mechanics are dominated by the cytoskeleton, which is the primary structural component of the cell, comprised of a variety of proteins that come together to form a latticework of supports [1]. Among the variety of proteins that comprise the cytoskeleton, the actin cytoskeleton is a key determinant of cell force production, mechanical integrity and structure, and mechano-sensation [1]. An essential yet often overlooked element of the actin cytoskeleton are the crosslinkers. These crosslinkers, just as in polymers, allow the actin network to interconnect a biopolymer network. One such crosslinker, alpha-actinin-4 (ACTN4), has been shown to transiently crosslink actin into bundles [7].

The viscous response of a biopolymer network can be quantified through creep, where a constant stress applied to the network results in an increasing displacement in time. For biopolymer networks with transient crosslinking, this creep is determined by the duration of binding, as there is no flow while bound. While the binding duration of most bonds decrease with applied force, there are some which display an increased affinity under load, and these are referred to as catch bonds.

Alpha-actinin (ACTN4) has been shown *in vitro* to display catch bond behavior, with a stress on the order of ~10 Pa being sufficient to engage this increased binding affinity, and acto-myosin contractility provides this stress *in vivo*. The mechanism behind this affinity is believed to be related to a cryptic additional binding site that is exposed under load, and a point mutation (K255E), which constitutively exposes this extra site should not display catch bond behavior. By examining the creep flow of WT and K255E cells as a function of contractile tension, we endeavor to characterize this catch-bond behavior in the cell.

In order to determine the role of ACTN4's role in cytoplasmic mechanics, methodologies of probing the cell's interior must be implemented. As previously stated, the methodologies available to researchers at the subcellular level, are OMTC and MTs [4]. These devices function by applying a magnetic field to magnetic particles and visualize their displacements. The displacement of particles in the magnetic field allows the researcher to measure the viscous and elastic response of the material in which they are embedded. The viscoelastic properties of the material are determined using complex mathematical models that fit the displacement of the embedded particles [8]. The

magnetic field can be modulated at various waveforms and frequencies, as the properties of viscoelastic materials depend on the frequency of sampling.

In this thesis, I analyze the passive and magnetically-induced movement of particles attached to or embedded within the cytoplasm of human cell lines. The introduced particles are synthetic iron oxide particles ranging from 0.2 to 4.6 μm. The bead displacement can be directly related to the cell's viscoelastic properties [8]. These properties can be resolved both spatially and temporally to quantify cytoplasmic mechanics. As this magnetic field can influence beads in many cells simultaneously, the method will allow high throughput of data acquisition. Using a well-established tracking algorithm, TrackMate [9], as well as custom written MatLab software, particles movement in cells are localized with subpixel resolution.

To investigate the role of ACTN4 in the mechanics of the cytoskeleton, we employ two cell lines: wild type (WT) ACTN4, and a heterozygous ACTN4 mutant (K255E). With these cell lines we would like to examine if binding affinity changes stress-relaxation *in vivo*. We hypothesize that cells exhibit variable stress-relaxation based on the contractile state of the cell, due to the catch-bond behavior of ACTN4. This study presents, to our knowledge, the first cytoplasmic creep measurements related to crosslinker binding kinetics and offers insight into the detailed cytoskeleton relaxation responsible for cell mechanics.

# 2. Background

## 2.1. Alpha Actinin: Cytoskeleton crosslinker

One of the main structural components of mammalian cells is the cytoskeleton network. The cytoskeleton is an assembly of structural proteins that act as both anchor and support for the cell to provide its shape and allow motility [1]. One of the main structural proteins in eukaryotic cells are the actin proteins, which are ubiquitous throughout these organisms. These globular proteins assemble in the presence of adenosine triphosphate (ATP) to become helical microfilaments or filamentous actin biopolymer (F-actin) [1]. The F-actin plays a critical role in maintaining the structure and movement of the cell through associated proteins, termed actin crosslinkers. The crosslinking proteins associated with actin help to form bundles or networks, which support and provides the cell's shape. The actin bundles are formed by short crosslinkers that keep the F-actin in tight, parallel collections termed fibers. The homodimeric alpha-actinin-4 bundling crosslinker has two actin binding domains at each end separated by a spectrin linker region (see Figure 1-Top). It has previously been shown that ACTN4 has increased binding affinity to F-actin upon exposing a cryptic second ABD in the CH2 domain through phosphorylation of tyrosine residue 265 [10], stress in the actin bundles [10], or the presence of a disease-causing point mutation of lysine 255 residue [11]. We hypothesize that due to the variability of binding affinity of ACTN4 based on its biochemical modification or mechanical deformation, bundles of F-actin will exhibit different mechanical properties, which is the core question explored in this thesis.

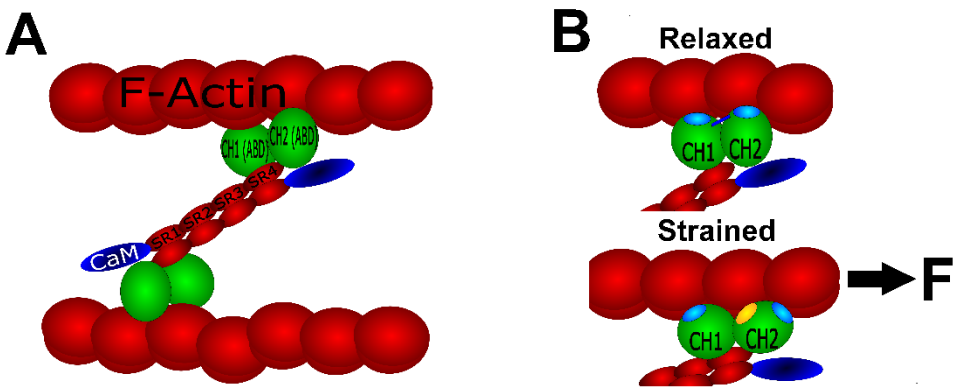


*Figure 1. Homodimer ACTN4 predicted structure.* ***A)****: ACTN4 homodimer "dumb-bell" structure. N-terminal CH domains which have two ABD (Green); Central linker region of 4 Spectrin repeats that form the dimer (Red); and C-terminus Calmodulin-like region (Blue) [10].* ***B)****: Top - ACTN4 homodimer (Grey) attached to F-actin (Red). Actin Binding Domains (Blue) attach to the F-actin in unstrained bundles. The Blue linker between CH1 and CH2 is formed by interaction of K255 and W147, which keeps the two regions in closed formation. Bottom - Strained bundles of F-actin expose cryptic Actin Binding domain in CH2 (Yellow) [7]. The exposure of this domain is thought to be due to breaking the K255-W147 linker due to strain in the protein or disease causing mutations such as K255E [10].*

*In vitro* networks of F-actin with various actin associated proteins have been a popular method of studying the bulk mechanical properties to understand the nature of these important structural components of the cells. These reconstituted networks helped demonstrated that the binding rates, binding energy, and the bond length of the crosslinker can drastically change how a network of biopolymers behaves macroscopically. Although the crosslinked actin biopolymer network is elastic in nature, as shown by Gardel *et al* [12], the microscopic properties affect its viscous dissipation. That is, the network undergoes rate-dependant relaxation that is highest at low rates of stress or strain frequencies near the crosslinking unbinding rate [13]. Taken together, the reconstituted networks of transiently crosslinked F-actin exhibit viscoelastic mechanical properties that vary with concentration of components and biochemical properties of the crosslinking partners.

When examining the F-actin transiently crosslinked with ACTN4 *in vitro*, similar mechanical properties to other crosslinked F-actin networks are observed. Yao *et al* [14] demonstrated that reconstituted networks of F-actin transiently crosslinked with ACTN4 behaved mainly like an elastic solid with a frequency-dependent network relaxation. As with Lieleg *et al* [13], the researchers noticed a scaling of storage and loss moduli of the network with increased ACTN4: F-actin concentrations, as well as the presence of stress stiffening in the network. The network's relaxation time was invariant to the change in concentrations and shown to be in line with the unbinding rate of ACTN4 [15] [16]. However, when the ACTN4 mutant K255E is used in a reconstituted F-actin network, the relaxation time shifts to a lower frequency, related to higher binding affinity, while the network exhibits a more solid-like behaviour at lower frequencies. This is consistent with established biochemical properties of ACTN4-K255E mutants [15] [16], which demonstrate an increased binding affinity of the mutant to F-actin mainly from the additional exposure of an ABD in the CH2 domain of ACTN4 (see Figure 1). The reconstituted F-actin network with transient crosslinker ACTN4's viscoelastic properties are therefore intrinsically tied to the biochemical interaction of these two binding partners.

*In vitro* models of transiently crosslinked F-actin networks demonstrate the physical and biochemical properties of the constituents, but what are the mechanical properties of the networks *in vivo*? Comparative studies in cells with and without mutant ACTN4 have shown that in cells, the mutant appears to have roughly 3x the binding duration of WT ACTN4, resulting in increased traction stress and work, decreased cell motility, increased cell spreading, and decreased intracellular movement [7]. The authors suggest that these differences are caused by the prevention of F-actin from sliding past each other within the

cells, which leads to reduced cell motility and doubling of the traction forces applied by the cell. This leads to the hypothesis that there is an “ideal” range of binding affinity for ACTN4, which allows the cell to undergo “dynamic solidification to allow movement” [7]. The understanding of where this range lies for the isoforms of ACTN4 is at the heart of this research.

Physiologically, when this mutant ACTN4 is present in renal cells (podocytes), it leads to focal segmental glomerulosclerosis (FSGS), which is the failure of the organ to filter urine properly [17]. The failure is thought to be due to the disruption of the F-actin cytoskeleton that lead to a loss of the interdigitating processes of these podocytes [11]. Podocytes extracted from mice with this homozygous mutant ACTN4 are shown to have a cytoskeleton that is brittle, disrupted, and easily detached during [18]. Cyclical strain applied to these mutant ACTN4 podocytes *in situ* has demonstrated that these cells have similar phenotypes of the FSGS pathology [18]. These studies demonstrate that the biochemical properties of ACTN4 play a critical role in the mechanical properties of the F-actin bundles in disease *in vivo*.

The evolutionary rationale behind such sensitive regulation of mechanics through minute cross-linker changes may lie in adaptation to mechanical stimuli. The cell is a complex assortment of chemicals and processes that come together to provide a physical entity, the cell, that can respond to its environment. The important components of the cell, such as the cytoskeletal network, provides the means of physically interacting with this environment. By modulating its biochemical activities, the cell can regulate stiffness of the cytoskeletal network to respond to its environment. Components, such as the cytoskeletal crosslinking proteins, allow the cell to modulate its response to environmental cues by

changing its biochemical properties. This change in biochemical properties and how a cell can modulate its response to the environment is at the crux of this study and at the very heart of the understanding of the cell.

## 2.2. Microrheology Methodologies

Rheology is an important measure of the mechanical properties of soft matter, such as viscosity, shear moduli, creep compliance, and stress relaxation. These data are obtained through the application of known strain, strain rate, and force regimes in order to determine the response of the soft matter. This is possible with shear rheology for bulk materials with uniform composition, however, for single cell or even tissues, it is no longer possible to assume homogeneity or even determine contribution of individual cells to the material properties. The reason for this is due to the application of millimeter strains and newtons of forces, largely outside the physiological ranges of these cells, which are in the micrometer length and nanonewton forces scales.

Micro-rheological techniques are means of applying and measuring forces and displacements at length scales appropriate for cells. Several types of methodologies have been developed within the past 50 years that apply pico- to nanonewton forces at nanometer to micrometer length scales: Atomic Force Microscopy (AFM) [19], Optical Tweezers (OTs) [19], Passive Microrheology (PMR) [3], Optical Magnetic Twisting Cytometry (OMTC) [20], and Magnetic Tweezers (MTs) [21]. All these methodologies have their limits of applicability and accuracy. For AFM, the application of forces to map the viscoelastic properties of the cells imparts deformation artifacts within the cell that affect the local properties of the probed cell [22]. For OTs, the main concern is the local heating and phototoxic effect of high powered laser light on living organisms over the

required time frame of the measurements [19]. The remaining methodologies, namely PMR, OMTC, and MTs are examined in more detail below for their merits and drawbacks.

Passive Microrheology is the measure of the displacement of colloidal probes in a continuous soft material through thermal forces alone [19]. An intensity-weighted centroid tracking algorithm [9] is implemented to measure probe displacement based on fluorescence microscopy image series with accuracy of approximately 10% of pixel sizes. The random displacement of the probe in time is quantified by the Mean Squared Displacement (MSD) (see equation (9)). The probe's MSD, $\langle \Delta r^2(t) \rangle$, can be related to the viscoelastic spectrum by way of the Generalized Stokes-Einstein Relation (GSER) [3]:

$$\tilde{G}(s) = \left. \frac{k_B T}{\pi R \langle \Delta r^2(t) \rangle \Gamma \left[ 1 + \left( \frac{\partial \ln \langle \Delta r^2(t) \rangle}{\partial \ln t} \right) \right]} \right|_{t=\frac{1}{s}} \quad (1)$$

where $k_B T$ is the thermal energy scale factor, $R$ is the radius of the probe, and $\Gamma$ is the gamma function. The viscoelastic spectrum is further related to the shear modulus, $G_r(t)$, by way of mathematical manipulation as described by Mason *et al* [3]. The storage, $G'(\omega)$, and loss moduli, $G''(\omega)$, are then determined from the unilateral Fourier cosine and sine transforms [3], respectively. Due to the complex nature of the cytoplasm, some assumptions of the passive microrheological methodology are not valid: the cell is not an isotropic, incompressible continuum, but most critically, it is not in a state of thermal equilibrium at frequencies lower than approximately 10 Hz. However, at frequencies above 10 Hz, the thermal forces dominate, and the viscoelastic properties calculated from PMR are accurate. To perform cytoplasmic PMR, the probe must be larger than the mesh

size of the network (~50 nm), and sufficiently small to probe small local area without disrupting them. Benefits of the PMR method are the simplicity of implementation and high spatiotemporal accuracy, limited only by the instrument's speed to quantify the probe's displacements, and the thermal-equilibrium frequency range of moduli measurements. Also, due to no stress being applied to the system through external sources, the methodology is always in the linear regime of the material. In the context of elucidating mechanical properties of the cell, this method allows the frequency dependent complex shear modulus in order to note the difference ACTN4-K255E has on the cell *in vivo*.

Although simple in application, PMR is limited to systems at thermal equilibrium; in cells, which are far from equilibrium, PMR can lead to qualitatively incorrect interpretations. Nevertheless, it has been shown that above 1-10Hz, cannot accommodate for a known force regime at frequencies less than 10 Hz, which is essential in determining the mechanical properties of soft matter at these lower frequencies. An alternative methodology that can measure material properties at any applicable frequency is active microrheology (AMR). AMR is the study of the flow of material under known force regimes at micrometer length scales, which allows the qualification and quantification of the material's response based on the frequency and magnitude of this force. For this study, we consider AMR techniques which use magnetic fields to apply piconewton forces to ferromagnetic and superparamagnetic particles. These techniques circumvent the frequency limitations of PMR and are free of heating and deforming artifacts from other AMR techniques due to minimal interaction of the magnetic field with the normal function of cells.

OMTC is an AMR methodology that can help quantify frequency dependent behavior of soft matter. An OMTC apparatus is a complex system of air core inductors used to displace magnetic particles by way of a magnetically induced torque [6]. A pair of magnetizing inductors are arranged in such a way to produce a strong, horizontal, uniform magnetizing field in a central region of interest when charged with a high voltage capacitor (see Figure 2-Right). The magnetizing field is pulsed at such a strength to induce a domain magnetization of the ferromagnetic particles. A second pair of inductors is arranged perpendicular to these magnetizing inductors to produce a relatively weak (0.1–10 mT) but highly controlled magnetic field which is perpendicular to the magnetizing field within the same central region of interest (see Figure 2). The strength of this field is direction related to the Biot-Savart Law for inductors where the modulated current supplied to the inductor is proportional to the magnetic field. The twisting field can be outputted as a steady current, sinusoidal wave of various frequencies (0.1 Hz to 2 kHz), or triangular waves of various frequencies.

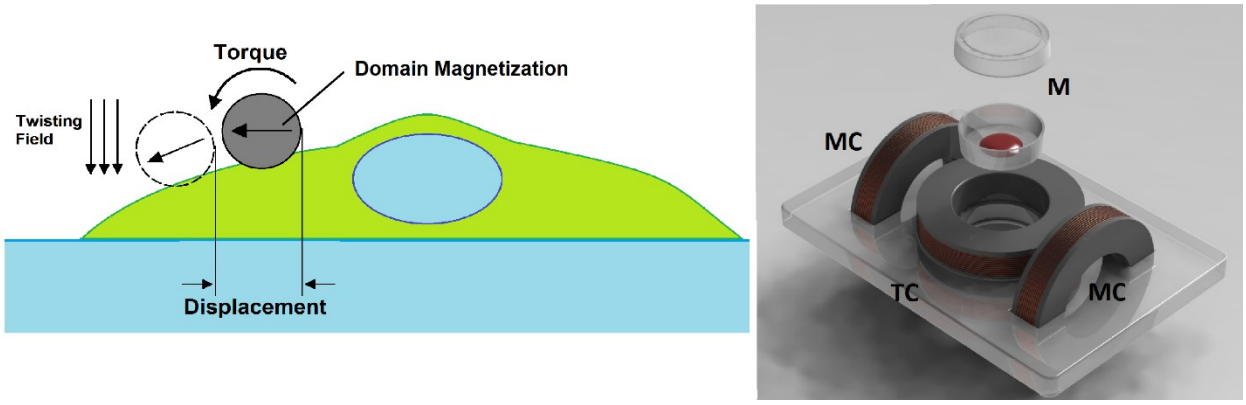


*Figure 2. Theory behind the displacement of particles influenced by OMTC device.* ***Left****: Twisting fields of OMTC. Magnetizing Field imparts a domain magnetization of the magnetic particle, while the Twisting Field imparts a Torque on the particle, which causes a lateral displacement.* ***Right****: OMTC Microscope Stage Insert. (M) MatTek dish with cells in media. (MC) Pair of Magnetizing Coils. (TC) Pair of Twisting Coils.*

A torque ($\vec{T}(t)$) can be imparted to the particles containing magnetic polarity, via the twisting magnetic field, that is at a specified angle to this domain by the following relation:

$$\vec{T}(t) = \vec{M} \times \vec{B}(t) = MB \sin\theta \tag{2}$$

where $\vec{M}$ is the domain magnetization of the ferromagnetic particle induced by the magnetizing field, and $\vec{B}(t)$ is the twisting magnetic field. The torque on the particles imparts a rotation that becomes lateral displacement when the particle is tethered at its base. The lateral displacements due to the rotation of the particles can be observed optically using light microscopy techniques and tracked using intensity-weighted centroid detecting algorithms like the passive microrheology method [9]. When a particle is attached to the surface of a material, the constrained displacement of the particle can be directly related to the materials rheological properties. Properties, such as the creep compliance, a measure of a material's deformation under prolonged stress, can be quantified by the ratio of displacement and applied force regime, as related in Equation (3):

$$J(t) = \frac{x(t)}{\alpha\, T(t)} \tag{3}$$

where $\alpha$ is the geometric factor of the particles as quantified by Mijailovich ***et al*** [23], $x(t)$ is the particle displacement in time, and ***T(t)*** is the volumetric torque regime being applied to the sample by the magnetic particles. To extract mechanical properties from the creep compliance, the mathematical model of viscoelastic materials shown in Figure 3 can be used to approximate the creep behaviour with the equivalent mechanical circuit and Equations (4)(5) [20] [24]. To apply this model to viscoelastic material, the assumption again must be that the material is a continuum – something only true at very small length

scales. However, when fit to previous studies' experimental creep compliance data, the model has good agreement.

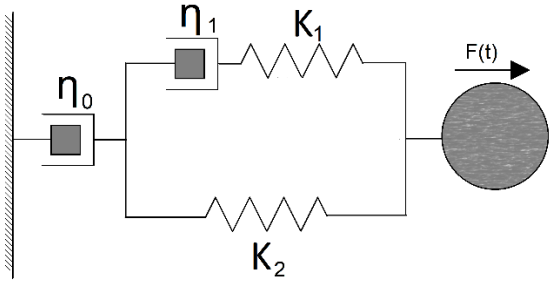


*Figure 3. Equivalent Mechanical Model of viscoelasticity behaviour of mammalian cells. Consisting of a Kelvin body in series with a dashpot. The springs are modeling the elastic behavior of the network attached to the particle, while the dashpots model the rate dependent viscous behavior of the network.*

This model can be simplified into Equations (4) and (5):

$$J(t) = \frac{x(t)}{\alpha\, T(t)} = \frac{1}{k_0}\left(1 - \frac{k_1}{k_0 + k_1} e^{-t/\tau}\right) + \frac{t}{\eta_0} \tag{4}$$

where

$$\tau = \frac{\eta_1 (k_0 + k_1)}{k_0 k_1} \tag{5}$$

The variables that are to be fit in the model are: the elastic components ($k = k_0 + k_1$) and the two dissipative components ($\eta_0$ and $\eta_1$). The behavior of a viscoelastic material upon the application of a step-stress, is for the material to undergo three distinct regimes; a quick elastic response proportional to the elastic properties of the network ($x = T/\alpha(k_0 + k_1)$ ); an exponential approach to a steady state; and a viscous flow at longer times [21] [24]. The benefits of this method are: a high throughput of data acquisition as a multitude of attached particles can be displaced simultaneously; the device can modulate its forces to remain in the material's linear range by increasing or decreasing the source amperage to the twisting inductors; and its turn-key implementation which allows for researcher to setup the OMTC on inverted microscopes with a standard microscope stage insert.

However, the OMTC requires complex mathematical modelling to understand the material properties of the sample. This assumes the cytoskeleton indirectly attaches to the particles via cytoskeletal associated proteins, including surface receptor integrins, in a bond that is stronger than the probed network's viscoelastic properties. In the context of the ACTN4 crosslinked network, this device can determine the creep response of the two cell lines to determine important properties of the network, such as relaxation times.

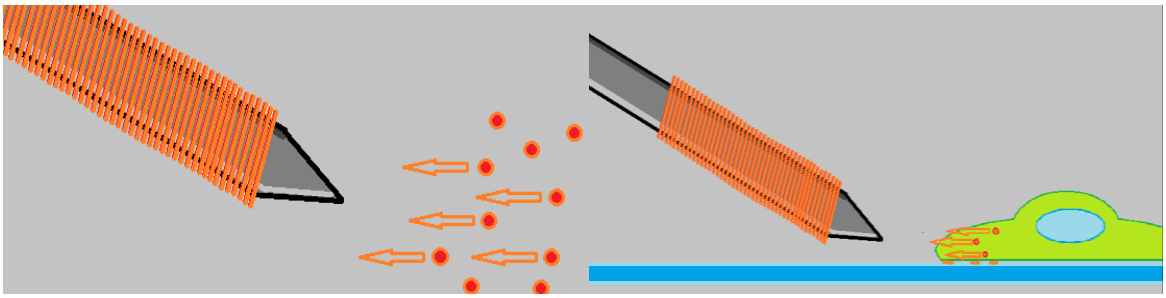

*Figure 4. Basic concept of MTs for use in Active Microrheology.* ***Left*** *– Calibration of MTs using ferrimagnetic or superparamagnetic particles in a fluid of known viscosity to understand the force being applied to each particle based on Stokes Drag.* ***Right*** *– The MTs are placed in close proximity of the cell to apply a known force regime to particles within a limited radial distance from the tip of the MTs. Displacement of the particles can be related to the mechanical properties of the cell based on the modified Standard Linear Solid (equation (8)).*

MTs are amongst the simplest of all the micro-rheological techniques available to researchers (see Figure 4). The design of MTs is an inductor, in circuit with an electrical power source, which is surrounding a ferromagnetic metal core of high magnetic permeability. These components come together to provide modulated magnetically-induced forces on particles [19]. The forces applied to the particles are in the pico- to nanonewton ranges in milliseconds to seconds, which is crucial for active micro-rheological measurements of soft matter. The forces are achieved by providing a magnetic field that is amplified by the magnetic properties of the metal core, in relation to the Biot-Savart Law:

$$B(t) = \mu_r \frac{N}{L} I(t) \tag{6}$$

where *B* is the magnetic field in time, $\mu_r$ is the relative permeability of the material at the core of the inductor, N/L is the ratio of number of turns of wire in the inductor by unit length, and *I* is the current in the inductor at a given time. The magnetic field between the magnetically charged metal core and the particle can be approximated as a dipole, which decays quadratically as in the relation, $\vec{B} \sim \mu_0 r^{-2}$ [25] The force on a particle can then be related to this magnetic field following a well-established mathematical model [26]:

$$\vec{F}_{mag} = \rho V \nabla\left(\vec{M}_0 \cdot \vec{B}\right) + \frac{V \chi_{bead}}{\mu_0}\left(\vec{B} \cdot \nabla\right)\vec{B} \tag{7}$$

where $\rho$ is the density of the bead, $\overrightarrow{M_0}$ is the initial magnetization of the bead, *V* is the volume of the particles, $\vec{B}$ is the applied magnetic field, $\mu_0$ is the permeability of vacuum, $\chi_{bead}$ is the magnetic susceptibility of the bead, and $\vec{B} \cdot \nabla$ is the gradient of the applied magnetic field. In order to make use of the MTs, particles must be placed within the cell through endocytosis [8], micro-injection, or attached to cell surfaces via ligand coatings interacting with integrin receptors [21]. The displacements due to the magnetic forces on the particles can be observed optically using techniques like the passive microrheology and OMTC methods. The magnetically induced displacement from step-stress regime on the embedded particles can be modelled as creep compliance of a viscoelastic network [8] [27] [28] [29]. This mathematical model of creep compliance for a viscoelastic material is like the OMTC modelling but with a basic geometric factor to account for sphere size ($g = 6\pi R$):

$$J(t) = \frac{g\ x(t)}{F(t)} = \frac{1}{k_0}\left(1 - \frac{k_1}{k_0 + k_1} e^{-t/\tau}\right) + \frac{t}{\eta_0} \quad (8)$$

The displaced particles can be fit to Equation (8) to determine the viscoelastic properties of the material, in much the same way OMTC data is analysed. The same assumptions are made for the model as well. Although, for sub-micron particles embedded within the cytoskeleton of the cell, the assumption of the material being a continuum is closer to being valid. Due to the magnetic origin of force on the particles, the experimental artifacts from the device, are much less as compared to other micro-rheological techniques. However, the MTs are dependent on the optical tracking of the particle displacements, and therefore are limited by spatiotemporal resolution of the optical system they are set up on. For the analysis of ACTN4's effect on *in vivo* cytoskeletal network, this device is capable of measuring the creep response of the two cell lines through modelling particle displacement.

Using active and passive micro-rheological methodologies have allowed researchers to analyze the complex nature of the cell in a variety of physical means, as described above. However, applying these methodologies on ACTN4 cell lines will allow us to quantify cross-linker contributions to cell mechanics, and understand how the binding affinity relates to network relaxation.

# 3. Methodology

## 3.1. Cell Culturing and Imaging

All cell culture work was performed using a Biological Safety Cabinet. The cell lines used in all experiments were: C1, a telomerase reverse transcriptase immortalized dermal fibroblast cell line expressing wild type Alpha-Actinin (WT ACTN4); and 193, a telomerase reverse transcriptase immortalized dermal fibroblast, which has a heterozygous mutant alpha-actinin (ACTN4-K255E) with a change in amino acid lysine in position 255 of the protein with Glutamic Acid [7]. Cells were cultured in culture media comprised of Dulbecco's Modified Eagle Medium (DMEM) supplemented with 10% (v/v) fetal bovine serum (FBS), and 1% (v/v) penicillin/streptomycin (P/S) (Wisent, QC, Canada) and incubated at 37°C with 5% $CO_2$ until needed, up to passage number 25 to limit senescence. For experiments, cells were harvested by incubating with trypsin 0.25% (v/v) in DMEM, centrifuged at 200x g, and resuspended in culture media. For visualization of the cells during imaging, the membrane of 193 cells were stained with CellTracker Green CMFDA Dye (Invitrogen, USA), and the membrane of C1 cells were stained with CellTracker Orange CMRA Dye (Invitrogen, USA) according to the manufacturer's instructions for suspended cells. Dishes for imaging were made with 35mm culture dishes with a cleaned #1 coverslip attached to the base of the dish with Silicone RTV Sealant #747 (Dow Corning, USA). The inside surface of the coverslip was functionalized with fibronectin using the following procedure: place approximately 250 µL of a crosslinking solution – 0.1M HEPES, 0.1 µg/mL Sulfo-SANPAH (Sigma-Aldrich, USA) – in the of the coverslip-dish; irradiate with ultraviolet light for 2 minutes, then remove the Sulfo-Sanpah;

add 250 µL of 2 µg/mL fibronectin:MilliQ-water solution to the center of the coverslip-dish; store at 4°C overnight.

Each cell line was plated on separate coverslip-dishes to a confluency of approximately 50 – 70% and incubated for 16 hours in culture media at 37°C with 5% $CO_2$. Particles for AMR were prepared based on the type of experiment. Ferromagnetic particles (Jeff Fredberg Lab, Harvard School for Public Health USA) with 4.6 µm diameter were prepared by vortexing with 21 µg/ml of small peptide-RGD (Arg-Gly-Asp, Peptides International, Ky, USA) at 4°C for two days in carbonate buffer (15 mM $Na_2CO_3$, 35 mM $NaHCO_3$, pH 9.4), before being washed and resuspended in phosphate-buffered saline (PBS) (Wisent, QC, Canada). Pink fluorescent (ex: 543nm, em: 560nm) 200 nm Superparamagnetic Iron Oxide Nanoparticles (fSPIONs) (Chemicell, Berlin, Germany) and green fluorescent (ex: 505nm, em: 515nm) 500 nm polystyrene nanoparticles (FluoSpheres F888, ThermoFisher, USA) were passivated with 150 MW poly-ethylene glycol in an EDC-NHS reaction described by Valentine *et al* [30]. Passivation was confirmed with a Zetasizer (Malvern Analytical, USA), to note the shift in zeta potential from negative to neutral of the particles.

Cells were incubated for 20 minutes with 50 µL of 2 mg/mL (w/v) 4.6 µm spherical ferromagnetic microparticles or for 3 hours with 10 µL of 2.5 µg/mL 200 or 500 nm fluorescent nanoparticles. Unattached particles were washed from the dishes by dripping PBS over the surface while it was angled 60° from table as the plate was rotated. The PBS was replaced with $CO_2$-independent Leibovitz media with 10% (v/v) FBS and 1% (v/v) P/S warmed to 37°C prior to imaging.

Coverslip-dishes were secured on a Leica TCS SP8 scanning confocal microscope (Leica, Germany) and heated using a home-built temperature regulating system that stabilizes ambient temperature to 37°C throughout the experiments. Image series were acquired using bidirectional resonance mode on the SP8, where the scanning mirrors of the microscope oscillate at a resonant frequency of 8 kHz for an image acquisition speed of 27 frames/second at a resolution of 512 pixels by 512 pixels. Brightfield image series were acquired using the Transmitted Light Photomultiplier Tubes (PMT-Trans) illuminated with 488nm laser light, while fluorescence images were acquired using the PMT with dye associated pre-sets of the tunable spectral emission filter: Cy-3 (for CMRA) and EGFP (for CMFDA and FluoSpheres). To acquire reflection images and series, the spectral filter was constrained to the green laser wavelength (488nm +/-10%) in order to capture the reflected surfaces where a sharp mismatch in refractive indices occurred. To confirm attachment or endocytosis of particles, a z-stack was taken prior to experiments and only cells with clearly localized particles above (for OMTC studies) or within (for PMR/MTs studies) were chosen.

### 3.2. Pharmacological Studies on Cells

Cells were incubated with the following pharmacological agent during the course of an experiment at 37°C and 5% $CO_2$: Cells treated for ROCK pathway inhibition were incubated with 25 μM Y-27632 (Sigma Aldrich, USA) in culturing media for 1 hour between experiments to deplete cellular contractility based as shown in previous studies [31] [32]. Cells treated for ATP depletion were incubated with filter sterilized 2 mM sodium azide and 10 mM 2-deoxyglucose in PBS for 1 hour between experiments based on previous studies [5].

### 3.3. Particle Tracking and Data Analysis

Particle tracking of image series was performed using the software Fiji [31] and the plugin [9]. The software uses a Laplacian of a Gaussian filter of each image in a series with an inputted variance from the user (approximately twice the size of the particles). A quadratic fit of the maxima found after converting the filtered image to Fourier space, allows the particles to be localized at the subpixel level. The spots are linked using a linear assignment problem, which processes the cost matrix based on the likelihood of the spots being linked in subsequent frames of a series. The linking is based on an estimated likelihood region that is selected by the user (depending on maximum velocity of the particles). The minimized cost of each connection provides a track for each particle's trajectory, which can be used in downstream data analysis via an outputted csv file. A custom written MATLAB (MathWorks, MA, USA) analyzes the trajectories of the particles and computes the data specific for the experiment.

### 3.4. Passive Microrheology

The cells used in passive microrheology experiments were prepare as described above with endocytosed PEG-passivated 500nm PS particles. Cells were imaged within a 60 s timeframe using SP8 confocal microscope using resonance mode scanning at framerates of 129 frames per second. Tracking algorithm TrackMate was used to track the displacements of the fluorescent nanoparticles. In order to quantify these passive forces, we make use of a quantity known as the mean squared displacement (MSD) or the measure of how much a particle has deviated from its previous position, and can be expressed by Equation (9) [5]:

$$MSD(\tau) = \langle \Delta r(\tau)^2 \rangle = \frac{1}{N}\sum_{n=1}^{N}\left(r_n(t+\tau) - r_n(t)\right)^2 \quad (9)$$

where $\tau$ is the lag time between subsequent positions, and $r_n(t+\tau) - r_n(t)$ is the displacement of the particles between two time points in two dimensions.

### 3.5. Optical Magnetic Twisting Cytometer

An Optical Magnetic Twisting Cytometer (OMTC) device (EOL Eberhard, Switzerland) was employed for a comparative study of the mechanical properties of the cortical actin network. The OMTC device is a microscope stage insert with two sets of inductors, which form magnetic fields that apply torque to the particles placed within the central dish holder (see Figure 2).

Cells were plated on coverslip-dishes, as described above, and secured in the central dish holder of the OMTC device (see Figure 2-Right) using Parafilm. Magnetic particles on the cells were initially magnetized using a high energy magnetizing coils in a direction parallel to the focal plane. A set of twisting coils apply a smaller twisting field perpendicular to the magnetizing field, which applies a torque proportional to the domain magnetization and the twisting field strength (see Figure 2-Left). The magnitude of the torque is based on the Biot-Savart Law of two air coil inductors (see Equation (6)), with constants of proportionality set by the manufacturer. The magnitude of torque is from Zhang *et al* [32] experimentally derived constant using the similar OMTC device and from the Fredberg lab experimentally derived constant using the same magnetic particles [20]. The relation of these constants to the applied torque was shown to be, $T(t) = C_{beads}C_{OMTC}I(t)$, where $C_{beads}$ = 2.08 Pa/Gauss, and $C_{OMTC}$ is 35.3 Gauss/A.

Fitting of the observed creep compliance (i.e.: the ratio of the displacement and applied force) is performed using a rigorous non-linear least squared fitting of Equation (4) using MATLAB's Curve Fitting Toolbox. The fitting was expressly limited to positive results for the four variables – as negative numbers are meaningless, and the starting points were appropriate to cells (elastic moduli of 1 kPa, viscosity of 100 mPa s). Fits that had an R-squared value of larger than 95% and a residual mean square approaching 0 were selected. Data fit with this model that were outside these ranges were not considered.

## 3.6. MTs Methods

### 3.6.1. Numeric Modelling

To achieve the highest forces at a given current, the MTs must be designed with the largest magnetic field gradient. To achieve this gradient, modelling was performed to ascertain the ideal dimensions of the MTs. Basic dimensions of the MTs components were based from Bijamov *et al* 2010 [33] numerical and experimental analysis of design parameters, in which they demonstrated the highest field strength and field gradient at the tip of the MTs. These design parameters included tip radius of equal to or less than 100 µm, and diameter of metal core of 6.35 mm. With the above parameters, the MTs field strength was modelled using the free software Finite Element Modelling of Magnetics (David Meeker, http://www.femm.info) with the following variations: mu-metal core with magnetic permeability of 50,000; tip radius; and distance of the inductor to the tip. Parameters were set to metal material for the tweezers core, non-magnetic plastic bobbin for the inductor, diameter of mu-metal core, and a 500 turn of insulated copper wire for the inductor. The basis of the software's modelling is from the time-invariant boundary problems of Maxwell equations [34] [35].

### 3.6.2. Building of MTs

The MTs were built using a mu-metal core (Mushield.com, NH, USA), 24-gauge copper wire (Digikey, MN, USA), and a 3-D printed inductor bobbin. The dimensions of the inductors and mu-metal core, were obtained from numerical analysis described above. The MTs mu-metal core was machined on a lathe with precise tolerances and filed with 1200 grit sandpaper with specific attention to the tip's radius of less than 100 µm. The inductor was turned by hand for a total of 656 turns in a length of 50 mm, which gives a coil density of 13120 turn/m. The inductor was secured to the mu-metal core using strong bond adhesive to limit variations in sequential experiments due to movement of the inductor along the core's length. A current limiting DC power source (Digikey, MN, USA) was used to provide a current through the Inductor from 25 mA to 5 A, in a simple circuit of an inductor in parallel with the DC power source (see Figure 5). To accurately move the MTs into desired position, the core was secured to a micromanipulator (Sutter MP-285, CA, USA) with XYZ displacement step sizes of 0.2 µm.

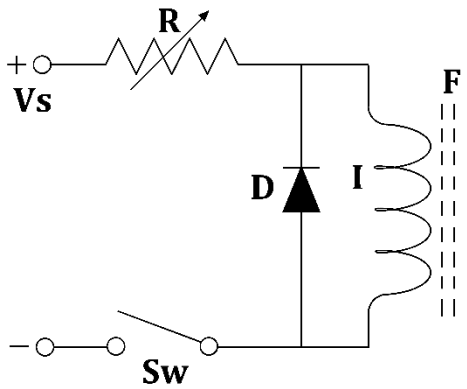


*Figure 5. Circuit design of ferrite core inductor for MTs. Variable resistor (R) is used to vary the voltage across the inductor, Diode (D) is used to suppress back emf upon discharge of the inductor, Switch (Sw) is in place to toggle the current through the system, the mu-metal core (F) is place within the inductor, and the voltage source (Vs) is from a direct current supply.*

### 3.6.3. Qualifying the MTs

The MTs' field strength was measured using a high precision Gauss-meter (Alpha Labs GM1-ST, Utah, USA). The field strength was measured from the central tip of mu-metal core touching the sensor, which was secured to a precisely leveled surface to give the zero offset of the field strength. The mu-metal core was attached to a micromanipulator that was precisely leveled and lifted vertically in small increments to accurately measure the field strength radially from the tip of the MTs. The MTs inductor was charged with incremental increases in current with each successive increase in height for consistency in measurement positions. The instrument is calibrated to give an accurate reading within 1% of the actual value.

### 3.6.4. Calibration of MTs

The calibration of the MTs was performed using a fluid of known viscosity with particles of known size. A colloidal suspension was prepared of super paramagnetic (200nm fSPIONS) or ferromagnetic particles (4.6μm) and non-magnetic fiduciary (500nm FluoSpheres) particles and 90%w/v glycerol: water solution with a dynamic viscosity of 300 mPa.s as measured using a conical plate rheometer (Anton Paar, Austria). The final concentration of particles was 2.5 μg/mL or 0.002% w/v. The colloidal suspension was vortexed for 30 seconds and sonicated for 1 hour (Branson Bransonic CPXH, USA) prior to use in experiments. The colloidal suspension was placed between two hydrophobically coated (Rain-X, TX, USA) coverslips separated by double-sided tape for a chamber that was approximately 100 μm. This was done to avoid the no-slip condition at the surfaces of the hydrophilic particles and the coverslips. The chambers were place on a confocal microscope (Leica TCS SP8, Germany) with the tip of the MTs positioned at the edge of the chamber in the field of view of the scanning area. High frame rate videos were

captured of the “On-Off” inductor charging cycles of the MTs (0.1 to 4 Amps) and the displacement of the colloids were tracked using a well-established tracking algorithm – TrackMate [9]. The displacements of the magnetic particles were drift corrected using the displacement of the non-magnetic fiduciary particles using a custom written MATLAB code. Based on the displacement and the frame rate of image acquisition, the instantaneous velocity can be determined. The force on the particles due to the magnetic field produced while the MTs are “On” can be calculated based on Stoke’s Law:

$$F = 6\pi\eta R v \tag{10}$$

where $\eta$ is the dynamic viscosity of the fluid, $R$ is the radius of the particles, and $v$ is the relative velocity of the particles. The distance of the particle to the tip of the MTs is directly proportional to the magnetic forces experienced by the particles based on the velocity profile of the particle.

### 3.6.5. Magnetic Tweezers on Live Cells

MTs were secured on the stage of a Leica confocal TCS SP8 microscope using adhesive tape and brought into proximity of the prepared culture dish using a micromanipulator as seen in Figure 6. The culture dish was secured to the microscope stage using adhesive tape to prevent drift while imaging. Prior to imaging, the cover of the culture-dish was removed to allow the tip of the MTs to maneuver within the dish using the micromanipulator with positional accuracy of 0.4 µm. The tip of the MTs was placed into the culture dish, in contact with the culture media, and then maneuvered into position within 25 µm a cell with magnetic particles using the brightfield of the microscope. The imaging software on the confocal was set to acquire 27 frames/second with a resolution of 512 pixels by 512 pixels and the pixel size was set to approximately 10% of the size of

the particles with zoom factor and objective selection (~400 nm and 10x objective for 4.6 µm; ~20 nm and 40x objective for 200 nm). An image series of the particles was acquired for approximately 3 minutes with the first ~1 minute with no current in the inductor coils (for PMR), ~2 minutes with 0.1 to 2 Amps of discrete charge through the inductor of the MTs (for AMR depending on required force and distance, see Calibration of MTs), and 10 – 15 seconds of recovery. The process was repeated under the above conditions within 25 µm of each cell until 5 or more particle displacement image series were acquired for each culture-dish. Tracking and analysis of particle movement was performed as described in Particle Tracking and Data Analysis methodology. Due to the nature of the experiment, an excess of culture media was used, and the entire process was limited to approximately 30 minutes per culture dish to limit for evaporation.

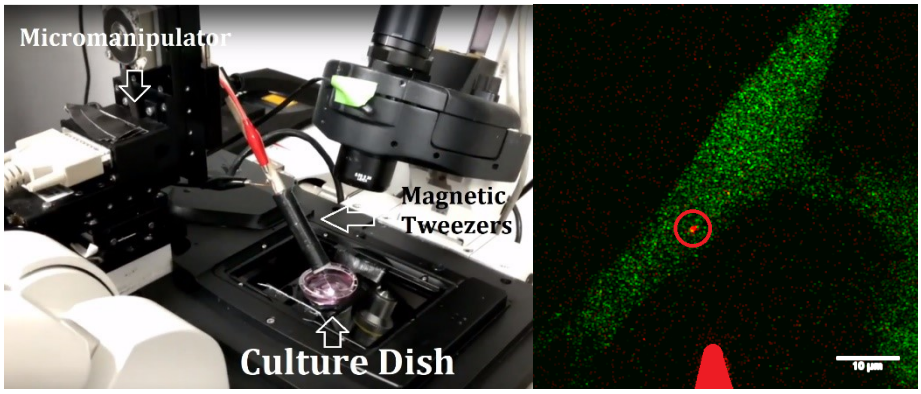


*Figure 6. Setup of MTs on Leica Confocal SP8 microscope.* ***Left*** *- MTs are maneuvered into position in the culture dish using a micromanipulator. The MTs are localized using the microscope and moved in XYZ-coordinates to a position of interest.* ***Right*** *– The tip of the MTs is in proximity of the bottom of the culture dish near a cell of interest. MTs tip (bottom – highlighted red) is brought to within 25 µm of the particle (red circled – fSPION) in or on a cell (green – CMFDA Dye) before charging the inductor coils. The forcing regime is kept on for a continuous 120 seconds and discharged immediately after.*

# 4. Results and Discussion

## 4.1. Passive Microrheology

Measurements of the cells' MSD were performed for both experimental cells lines in order to determine notable differences between the two isoforms of ACTN4. MSD is the measure of a particles' average displacement over a given time period [36]. In simple materials, these displacements are driven by bombardment of thermally agitated molecules as they move in the material, which is a measure of the flow of the material under thermal equilibrium. In complex viscoelastic materials, such as the cytoplasm of a cell, the MSD exhibit multiple power-law time dependencies, which is an indication of an active driving force as well as a thermal force, expressed as $\langle \Delta r^2(\tau) \rangle = A\tau^{\alpha}$ [36]. On a log-log plot of lag time and MSD, the power-law exponent becomes the slope of these displacements and is a measure of the diffusion of particles. In an active system, such as the cytoplasm, the exponent ranges from 0 to 2, where 0 is essentially a solid (i.e.: no diffusion); less than 1 is sub-diffusive or hindered diffusion; and above 1 is super-diffusive or active transport. These measures are an indication of the mode of displacement at various timescales, however, it does not provide the actual mechanism of these displacements [36].

Tracking of the particles was tested to have a resolution of approximately 15 nm measured by tracking the displacement of a particle adhered to a coverslip (Figure 17). The particles were tracked inside the cytoplasm of each cells line by confocal microscopy after being endocytosed by the cells. Although highly accurate, the methodology suffers from low throughput due to the requirement of high spatiotemporal resolution, which is mitigated by the quick and simple nature of the experiment (see Methodology). The

endocytosis of the particles introduces the confounding issue of a vesicle surrounding the particles, which could provide error in the measurement. This error is in the underestimation of the particle size in the measurement, as well as increased particle displacement due to the potential active transport of these vesicles as cargos. To account for the error of active displacement, particles that are diffusive or sub-diffusive are chosen, as those that are super-diffusive are currently being displaced by active transport [36]. As for the particle size underestimation, the error introduced is assumed to be small compared to the overall size of the particle and thus it is ignored for this study.

The MSD of ACTN4 cells show a great deal of information about the physical nature of each cytoplasm (see Figure 7-Left). The cytoplasm of WT ACTN4 is sub-diffusive at long timescales and transitions to this state at timescales of less than 1 s. While in the presence of Rho kinase (ROCK)-inhibitor, the cytoplasm of these cells become closer to diffusive at long timescales and the transition to this state happens at longer timescales as compared to untreated samples. These results are consistent with a more solid-like cytoplasm over longer timescales due to the interruption in the ROCK pathway as the cell becomes less contractile and less motile [31] [37]. An Increase in timescales of transition implies a solid-like behaviour for longer, consistent with less fluidity in the network from downregulation of myosin activity and F-actin bundling and formation.

MSD of ACTN4-K255E cells show that they have marked differences in cytoplasmic properties as compared to WT ACTN4 (see Figure 7-Right). The cells were shown to have equivalent diffusivity from treated to untreated samples, while the transition from solid-like to liquid-like behavior is at shorter timescales. As in the WT ACTN4 cells,

this is consistent with ROCK-pathway inhibition, where the cytoplasm shows a solid-like behavior over long timescales due to cytoskeletal regulation interruption. However, untreated ACTN4-K255E cells were solid-like for even longer timescales from treated samples. The potential reasoning behind this is that in untreated cells, ACTN4-K255E crosslinkers remain bound for longer due to its increased binding affinity, while in the treated cells the F-actin is no longer able to form into bundles and ACTN4 is no longer recruited to stabilize these structure [37].

As previously reported [7], the ACTN4-K255E cells show a delayed transition from solid to liquid behavior, when comparing the MSD to WT ACTN4 of untreated samples (WT ACTN4: 0.6 s; ACTN4-K255E: 2.8s). This is thought to be due to the 3-fold increase in binding affinity of the mutant as it has been shown *in vitro* [15]. The increased binding affinity of ACTN4-K255E translates to slower dissociation rate as compared to the WT ACTN4, which may manifest itself as the delay in diffusive transition seen here. When comparing the treated samples of WT ACTN4 and ACTN-K255E, an almost identical MSD trace is observed. The similarity in the two traces suggests a close link between the two cell types, as when the active components of the cell is abolished, a common viscoelastic behavior emerges, and that the differences between the two untreated samples are due to the cytoskeletal components of each.

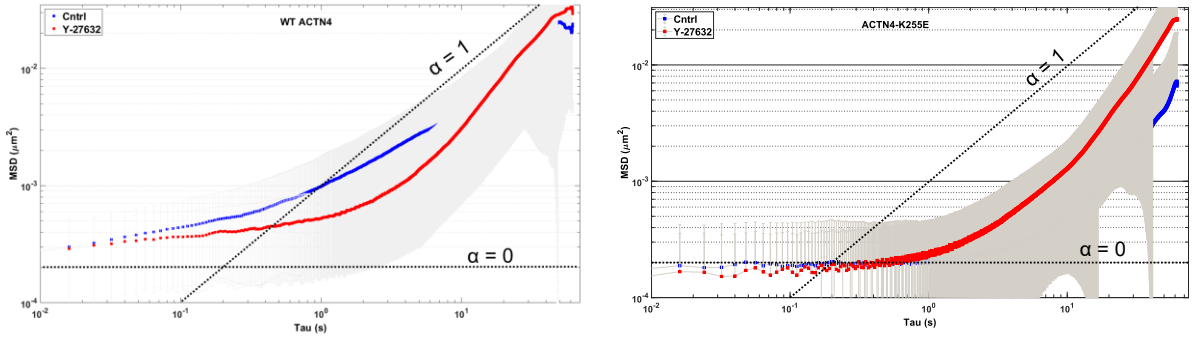


*Figure 7. Mean Squared Displacement of WT ACTN4 cells and ACTN4-K255E cells before and after ROCK-pathway inhibition treatment. Scaling exponent α is the measure of time-dependent movement of particles, where 1 is viscous fluid and 0 is a solid.* ***Left*** *– MSD of untreated WT ACTN4 cells show a less diffusive cytoplasm as compared to treated cells. Cells transition to diffusive movement at longer timescales from untreated to treated samples.* ***Right*** *– ACTN4-K255E cells MSD exhibit similar diffusivity from untreated to treated samples. Transition to diffusive movements happens at earlier time scales in treated samples as compared to untreated. Error bars are standard error of the mean.*

When using the PMR methodology to convert the MSD into complex shear moduli, a limitation is clear – the method is only valid for frequencies where the assumptions hold true. These assumptions are that the material is an isotropic homogeneous continuum, it is at equilibrium, and that thermal forces drive the motion of the probe particles [3]. In living organisms, this becomes more complicated as the cells are in a non-equilibrium state where dynamic active forces within cells provide the movement of cytoplasmic components. These active forces dominate frequencies lower than 10 Hz, while the passive forces from thermal energy dominate at the frequency ranges above 10 Hz. By using probes larger than the mesh size of the network but small enough to sense the network as continuum, the theorem can be applied to cells.

WT ACTN4 and ACTN4-K255E cells are shown to be primarily weak elastic solids (see Figure 8). A doubling of the storage modulus is apparent in the two cell lines across most frequencies (WT: ~15 Pa; K255E: ~35 Pa), which is consistent with the mutant

induced stiffening of the F-actin network seen *in vitro* [14]. ACTN4-K255E cells exhibited a decreased in fluid-like behavior (loss modulus) as compared to cells with the WT, as it has been shown that the cytoskeleton is less motile from a higher binding affinity and therefore less dissipation through F-actin sliding [7]. When comparing the effect of ROCK-pathway inhibitor on the cell lines, there is very little effect on the storage modulus, while there is a significant effect on the loss modulus. As seen in the MSD, WT ACTN4 cells became less fluid-like (decreased loss modulus) in the presence of ROCK-inhibitor, while ACTN4-K255E became more fluid-like. This suggests that the elastic nature of the network is conserved, but its dissipative nature is changing. For WT cells this may be due to the lack of F-actin sliding from myosin activity to allow dissipation of stress. Although for K255E, this may be due to the freedom of the F-actin to move as it is no longer in large networks of stress fibers. As the storage modulus does not change drastically in either condition for each cell line, the assumption is that ACTN4 is still capable of forming weakly elastic networks with the F-actin but not in a cohesive cell-wide network.

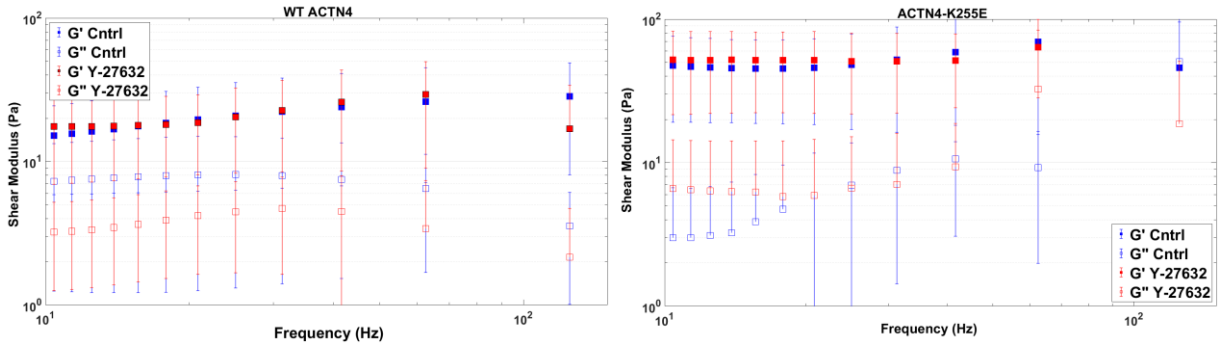


*Figure 8. Passive Microrheology of WT ACTN4 and ACTN4-K255E cells before and after ROCK-pathway inhibitor treatment.* ***Left*** *– Cells exhibit a more solid-like cytoplasmic behavior in the presence of ROCK inhibitor across all frequencies. Loss modulus is decreased considerably in treated samples.* ***Right*** *– The cytoplasm of treated cells have no marked difference in the storage and loss modulus from untreated cells across most frequencies. Error bars are standard deviations.*

The overall physical changes occurring in cells with mutant ACTN from WT, is a more solid-like cytoplasm for longer timescales. This transition is assumed to occur at timescales in line with the unbinding rate of the ACTN4 mutant. Due to this increased binding affinity the cytoplasm has a higher elastic nature. As this methodology is not valid at timescales lower than 10 Hz, another methodology is required to discover the relaxation at slow frequencies. The active forces induced by OMTC methodology is within the frequency range of this study, as a step-stress can be applied at a slow rate to probe the slow relaxation times of the ACTN4 network *in vivo.*

## 4.2. Optical Magnetic Twisting Cytometry

Previous studies have shown limitations in the OMTC technique [20] [38] [39], which include the local remodelling of the actin structures at the cell-particle interface, variability in the particle size, magnetic susceptibility, and cell-particle interaction. For this study, the local remodelling of the actin structures does not pose a limitation as these structures are required for the analysis of the creep compliance of the network, regardless of the concentration of actin cytoskeleton. However, when using the approximated volumetric torque as measured, we introduce confounding errors into the measurement of the creep compliance due to the variability in the size and magnetite distribution within each particle. The error is thought to be mitigated through use of embedding geometric factor discussed by Mijalovich *et al* [39], which accounts for the size of the particles and the cell-particle surface interaction. This property is experimentally assessed using reflection mode of a confocal microscope to measure the cell-particle interaction. An image processing algorithm is used to measure the full-width at half maximum of the particle size and compare to the full-width at half maximum of the cell-particle surface reflection. This ratio

of sizes is termed the embedding factor. This ratio is a self-check, as all particles who are below a 10% embedding factor are considered to have insufficient binding interactions of their coated ligands and the cell surface receptors [20] [39].

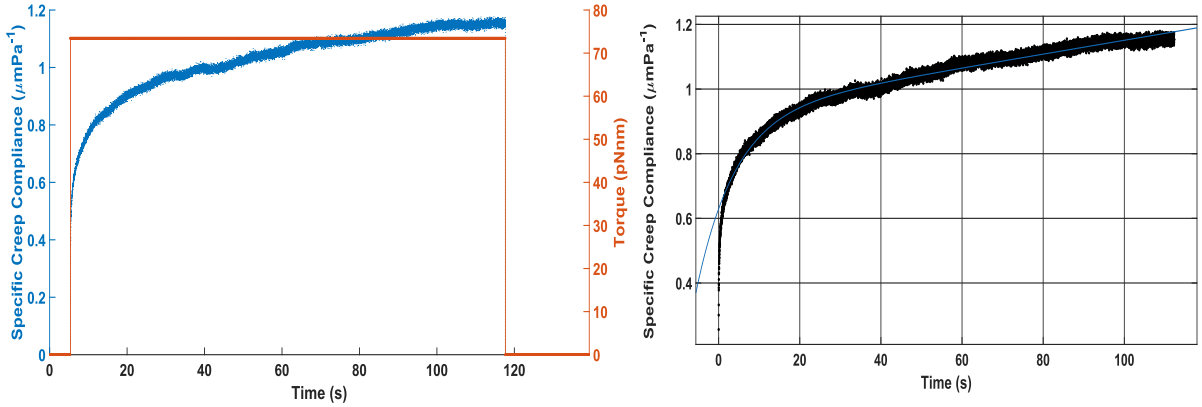


*Figure 9. Representative creep compliance curves of particles attached to cells using OMTC. Left - Force regime (red) and representative creep compliance (blue) of ACTN4-K255E cell. The creep curve shows the characteristic instantaneous elastic response, followed by a slow relaxation, that leads to a viscous flow regime. Force is assumed to be a step function although has been approximated to vary by less than 10% [20]. Right - Fit of the creep compliance based on Equation (4) showing good agreement with data.*

Twisting of the particles by OMTC results in a translation of the particles based on the compliance of the underlying cortex as seen in Figure 9, which is a representative creep compliance curve of a particle attached to a 193 cell. The creep compliance can further be analyzed using equivalent mechanical circuits of the cell-particle interaction (see Figure 3). When the data is fit to the Equation (4), there is good agreement with the mathematical model of creep compliance. This is achieved using rigorous fitting parameters (see Methodology), which allows us to obtain the cell's mechanical properties and thus the relaxation times of the network (see Equation (5)). As this method makes use of a fit to a mathematical model to determine creep compliance, there is high variability in the live cell data that can be compounded in the results. Each cell may have variable as-fit viscosities and moduli that would vary the data considerably. A sample size

that is large enough can potentially accommodate for these variabilities, but this size is unknown. Previous researchers have seen considerable variability for the fitted parameters in more than 35 samples, which underscores the benefit of this high-throughput methodology.

To understand the role of ACTN4 in the relaxation of the actin network in cells, the OMTC was applied to the WT ACTN4 and mutant ACTN4-K255E cell lines before and after ATP depletion using sodium azide and deoxyglucose (see methodology). The rational of this experiment is that untreated cells will allow for normal fluidity of the actin structures by way of myosin II motors at the long sampling timescales (>1 minute) as seen in previous studies [7]. However, in the ATP depleted cells, the network has no means of actively straining the network, therefore the network is thought to be relaxing from viscous dissipation associated with binding kinetics of the unstrained crosslinkers (i.e.: non-catch-bond behavior of WT ACTN4 and strain insensitive behavior in ACTN4-K255E). The comparison of the two conditions in the two cell lines allows us to determine the contribution of the different binding kinetics in strained and unstrained networks *in vivo*, to mechanical properties from the fit creep compliance.

Each OMTC experiment had a sample size of 10 cells for each condition, and there were four separate experiments performed to provide an abundant sample size. As the experiment required extended incubation (1 hour), the same cells were not used for pre-treatment as post treatment for the analysis of creep compliance. This method is less robust than applying the twisting on the same particles before and after ATP depletion due to the inability of seeing the effect of treatment on a cell's mechanical properties. However, the sample size has a large number of cells (10+ cells per condition), which

allows us to mitigate cell-to-cell variability and provide sufficient buffer for data that does not meet the fitting criteria discussed above.

When the data from creep compliance of the ACTN4 cell lines were fit to the creep compliance model (see equation (5)), the relaxation times were determined from the fitted variables (see Figure 10). Despite the sample size, the variability of the relaxation times was considerable for most conditions, indicating a large variability within the as-fit moduli and viscosity of the cells probed. Previous studies also noted a large variability in model parameters within their sample size, suggesting the nature of the fitting method is highly variable [8] [20] [21] [27].

The WT ACTN4 cells had no significant difference between untreated (9.8 +/-6.4 s) and treated samples (6.8 +/-5.2 s), suggesting that there was no change in the relaxation times of the pre-strained and non-strained network (untreated vs. treated, respectively). *In vivo*, during ATP depletion, the cell is expected to have an unstrained network due to decreased myosin activity, thus, the WT ACTN4 crosslinkers will have a decreased binding affinity of the crosslinkers as the cryptic actin binding site is no longer being exposed. However, if this were true, the strained network (WT ACTN4 – C1) would exhibit higher relaxation times than the unstrained network (ACTN4-K255E – 193) due to the increased binding affinity from the exposed third actin binding site. The results do not demonstrate this catch-bond relation of ACTN4 with the as-fit relaxation times of the untreated and treated cells expressing WT ACTN4. The results could be confounded by incomplete ATP depletion in cells as well as the high variability in the as-fit relaxation times. The variability in the fit parameters is a noted issue with creep compliance data analysis and has been difficult to reconcile in these studies. Previous studies have

discussed possible location dependence and probe size and speed dependence for the distribution of moduli and viscosity as the cause of the heterogeneity within the cytoplasm of cells [8] [40].

The observed relaxation times of untreated and treated ACTN4-K255E cells (193) did not show notable differences (2.3+/- 2.4 vs 6.9 +/- 14.5 s, respectfully). However, the variability of the relaxation time of the treated sample blur any comparisons between the sample set. Again, the variability in the as-fit parameters of the sample data causes some concern about the validity of the methodology. Despite variability in the data, the relaxation times of ACTN4-K255E networks are shown to be invariant to network strain of the cell. This is thought to be due to the permanent exposure of the cryptic actin binding site, which abolishes the catch bond behavior seen *in vitro* [14], causing the binding kinetics of ACTN4-K255E to be unchanged in both conditions.

In all cases, the network relaxation varied considerably from previously reported time scales (WT 29 ± 13 s, and K255E are 86 ± 29 s [7]), which suggest the network is not relaxing due solely to the binding rates of ACTN4. Alternatively, the variability in the as-fit mechanical properties required for the methodology introduced considerable error that confounded the results.

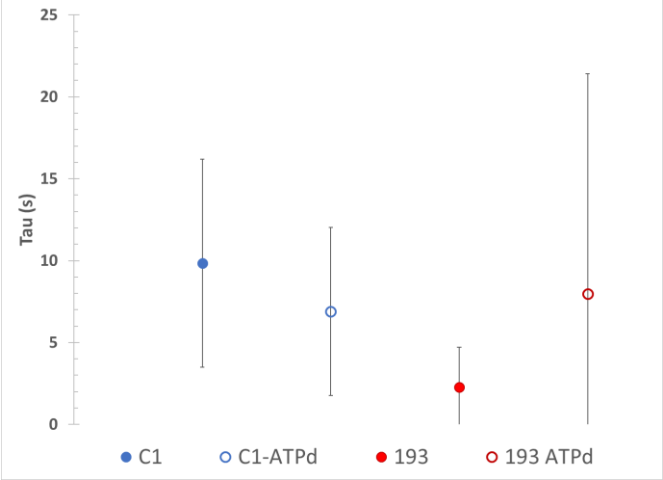


*Figure 10. Calculated relaxation times from as-fit parameters for C1 (WT ACTN4) and 193 (ACTN4-K255E) cells with and without ATP depletion. Cells were probed before and after ATP depletion. No significant difference relaxation times were observed between ACTN4 WT and K255E under control conditions. A significant increase in relaxation time was observed for ATP depleted ACTN4-K255E cells as compared to WT ACTN4 in either condition. Error bars are standard deviation.*

The particle displacements under the influence of continuous torque from the OMTC device were highly variable and exhibited significant off-axis displacement from rotation direction (see Figure 16). The highly variable displacement can be due to the non-uniform tethering of the particles to the surface of the cell, which causes the particle to displace in a path as it achieves the full extension of the slack within the cell-particle tether before pulling on the cell's viscoelastic cortex. A brief torque was applied to the tethered particles prior to creep displacement to remove this potential of slack within the tether (10 s), however the extension was still highly variable (0.15 to 2.51 μm). The displacement of the particles perpendicular to the axis of rotation was another confounding factor as it denoted a cell axis dependence. As the axis of rotation deviated from the major axis of the cells, the particles had larger off-axis displacement. This is in line with the difference in the major-minor axes' elastic moduli, which would cause non-linear displacement of particles pulling upon this network.

Despite being a non-invasive high-throughput methodology, OMTC suffered from significant drawbacks of creep compliance fitting variability. The particles attachment to the cell was inconsistent throughout the experiments, as particles with similar embedding factors had a variety of elastic responses in their creep compliance curves (data not shown). As the elastic response is a measure of the cell's elastic moduli, the variation in this response leads to inconsistencies in the as-fit parameters, and thus introduction of error in the calculated relaxation time. Additionally, the nature of the force is poorly defined as the torque on the cell does not match any computational model previously reported [32] [23], due to the discontinuous and anisotropic nature of the network [8]. As this force has a direct connection with the creep compliance, variable or wrong assumptions of the force will cause variabilities in the as-fit parameters of the cell's mechanical properties.

To better define the force on the cell and to control for the variabilities in the methodology, MTs were implemented to measure the relaxation times of ACTN4 networks *in vivo*. MTs have the advantage over OMTC device as the tunable force is radial to the tip and well defined, provided proper calibration. Due to the lateral natural of the force, tethering of the particles to the cell surface is no longer required, which limits the variation in variability in embedding and non-uniform tethering. Overall, the confounding factors, which causes variability in measurement, are controlled for by default when implementing the MTs.

## 4.3. Magnetic Tweezers

In order to achieve a tunable force on magnetic particles, the MTs must be built around the optimisation of the parameters which maximizes the magnetic field strength. Lending from the work done by Bijamov *et* al [33], which outlined optimal sizes of the MTs, the

modelling was performed using 6mm core diameter, tip radius of 200 um, and length of 10 cm. These measurements were shown to provide the largest magnetic field strength, which provides a basis for further analysis of MTs optimization. The parameters modelled for the MTs in this study (as described above), demonstrated that the highest field strength could be achieved through an inductor that was as near to the tip as possible and a fine tip of less than 100 μm (see Figure 11). The distance of the inductor from the tip of the MTs had the most dramatic effect on the magnetic field strength, where a doubling of the distance caused a 1.7-fold decrease. Subsequent displacements of the inductor had a less pronounced effect on the magnetic field strength (1.2-fold decrease). This is due to non-uniform domain magnetization of the core material across its length, which highlights the importance of the placement of the inductor in relation to the tip of the MTs.

The decrease in the MTs tip radius had an overall positive effect on the magnetic field strength with each decrease in radius (see Figure 13-Right). With each decrease in tip radius, from 100 to 25 μm, the magnetic field strength increased in a quickly decaying exponential of magnetic field strength. The explanation of this is in the tip geometry of the MTs. As the tip is decreased in radius, the magnetic domains within the material are less numerous, therefore the magnetic dipole of each domain is more likely to be in the same orientation and contribute to a higher field strength. Additionally, the gradient of magnetic field increased in the same fashion as the tip radius decreased, from 0.51 to 0.82 T/m, with the most significant increase between 100 to 90 μm tips (0.51 to 0.72 T/m). The increase in gradient in this case is due to the decrease in area of the tip, concentrating the magnetic field to a smaller area. Taken together, the tip geometry is understandably

a crucial design parameter in order to achieve the magnetic field strength and gradient required to displace microscopic particles.

Beyond complex modelling, the basic model of an inductor as described by the Biot-Savart Law, (see Equation (6)), is central in the design of a high magnetic field MTs. To obtain the highest field, $B$, one can see that increasing $\mu_r$, the ratio N/L, and the current passing through the inductor will have a positive effect on the magnetic field strength. To increase $\mu_r$, one must choose a material for the core that is highly permeable to magnetism, which mu-metal is amongst the highest in terms of relative permeability [41]. Additionally, mu-metal has a very low remnant magnetization, the effect of a having a non-zero magnetic field strength despite there being no current in the inductor. This is important to limit low level forces affecting the force regime experienced by the particles when they are in the proximity of the MTs. Another important factor is the ratio of turns to length as a denser inductor will allow for the largest magnetic field strength. Lastly, the magnetic field strength must be able to be tuned based on the amount of current going through the inductor, which can be applied in any current source pattern from pulsatile, sinusoidal, or triangular waves.

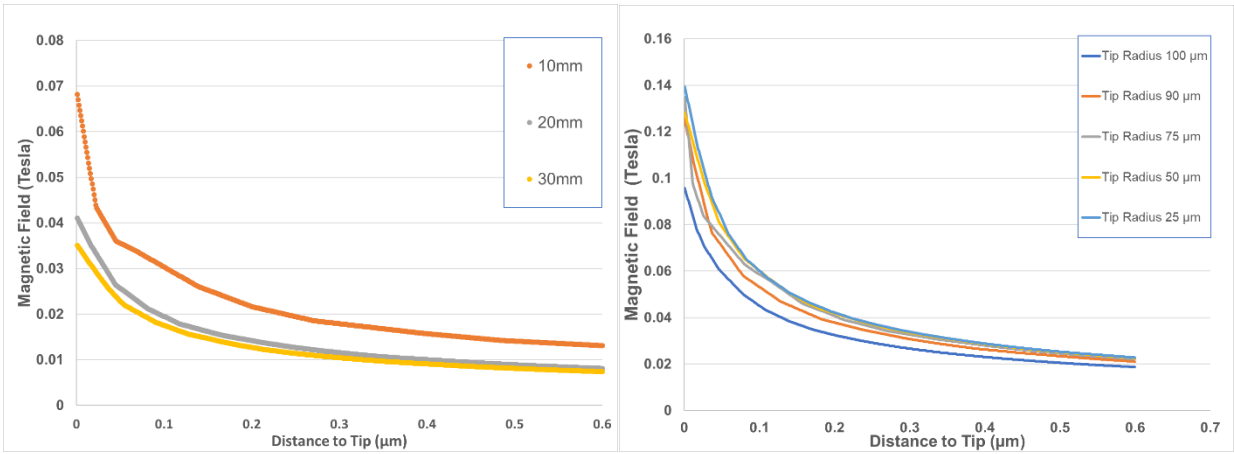


*Figure 11.* ***Left*** *- Magnetic Field radially from the tip of MTs with an inductor that is 10mm, 20mm, or 30mm from the tip (inductor tip kept at 200µm).* ***Right*** *- Magnetic field radially from the tip of the MTs with 100µm, 90µm, 75µm, 50µm, and 25µm tip radii (inductor kept at 10mm from tip).*

Despite rigorous modelling of the MTs to define optimal parameters for high magnetic field strength, the physical assembly of the design could not be adequately implemented to these parameters. Specifically, the inductor could not contain too many turns over a narrow length and also be close to the tip. The reason for this is due to interference of the MTs with the condenser head of the microscope (see Figure 12). Additionally, the machining of the MTs mu-metal core was not successful in achieving a lower than 100 µm tip radius, which would have allowed for higher gradients and magnetic field.

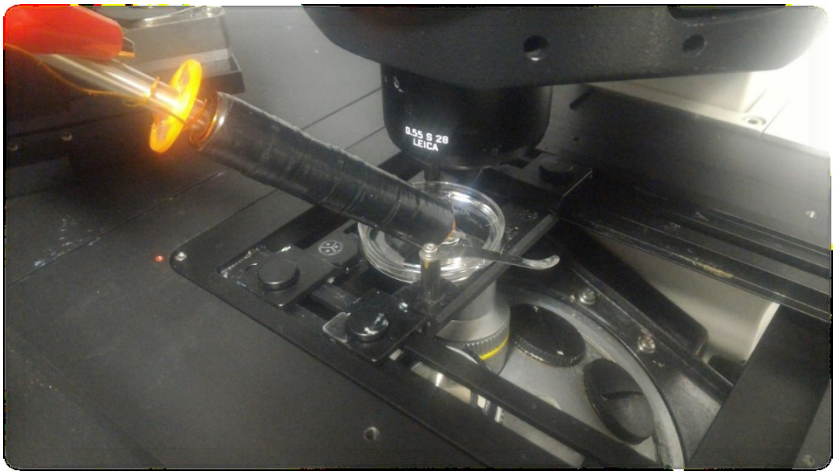

*Figure 12. Magnetic Tweezers as built in position for experimentation on a Leica SP8 Confocal Microscope. The interference of the Condenser Head of the confocal microscope with the MTs limits the entry angle into the culture dish, the distance of the inductor to the MTs tip, and the linear density of the inductor.*

The MTs were tested for their ability to hold a magnetic field and show a high gradient near the tip as well as tunable Magnetic field strength (see Figure 13). The MTs measured gradient was in line of the experimental ranges of previously published works [21] [8] [42] [38] of 3000-15000 T/m. Of particular interest is the increase in levels of gradients with increasing source current, which demonstrates the non-linear magnetic permeability property of the mu-metal core. The gradient can be assumed to reach some maxima as the inductors field strength increase, however this was not performed for safety reasons as the burnout current for the gauge of wire used was attained in the measurements, as well as high heat flux from resistance heating in the wires of the inductor. The magnetic field strength was shown to increase exponentially (see Figure 13-Right) as the MTs were held close to the Gauss-meter and the current was increased. An approach to saturation was apparent in the magnetic field strength as the mu-metal approached its maximum, which is its intrinsic material property.

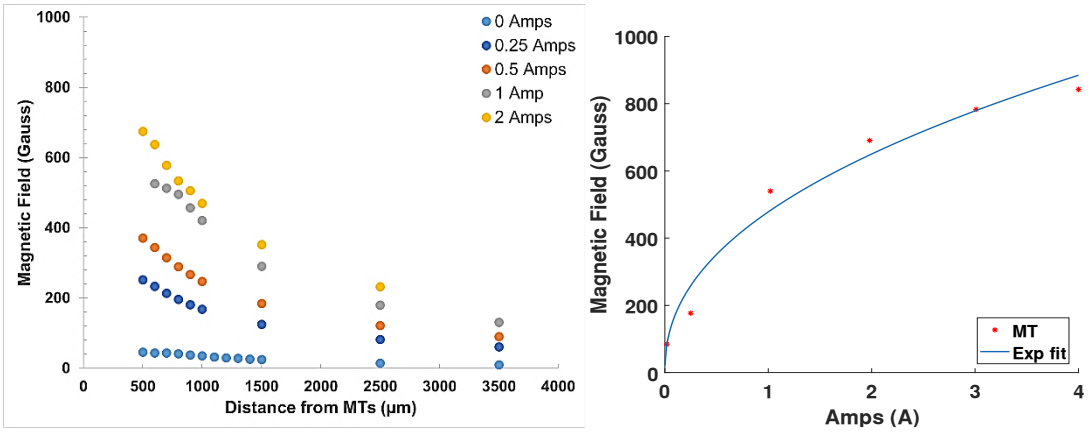


*Figure 13.* ***Left*** *- Magnetic Field Strength of the MTs based on vertical distance from Gaussmeter. Increase of the magnetic field strength is roughly linear and follows equation (6). A remnant magnetization is apparent at when no current is charged in the inductor, which is characteristic of ferromagnetic material.* ***Right*** *- Magnetic Field strength of MTs as a function of inductor Current. Exponential fit is to demonstrate approach to magnetic force saturation plateau as the mu-metal is magnetically forced to saturation by the inductor.*

Due to the nature of the calibration technique implemented (see Methodology), we required a colloidal solution of magnetic and non-magnetic particles in order to drift correct the trajectories of the magnetic particles, as the displacements from diffusion are convolved with the magnetic force displacements. The drift-corrected displacements, and therefore the instantaneous velocities of the particles (see Figure 14), are assumed to have a linear relation with the magnetic force on the particles as seen in Equation (10). A representative force regime of the MTs while being charged with 1 A current is shown in Figure 15. The forces applied to 200 nm fSPIONs are similar previous studies of MTs [26] [8] [27], and ranges from 10 to 50 pN at a distance of 50 to 20 μm from the MTs tip (see Figure 15). The force exhibits a second order polynomial fit as the particles approach the MTs tip, which is in line with the mathematical model proposed by Shevkoplyas *et al* [26] (see Equations (7)(10)). This validates the dependence of the force with the gradient of the magnetic field as both components of Equation (7) are based on this property of the

field. Therefore, the critical component in the design and implementation of MTs is the magnetic field strength gradient.

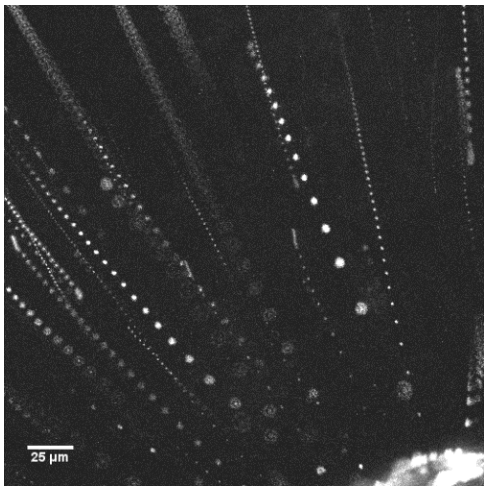


*Figure 14. Max projection from image series acquired on a Leica Confocal SP8 shows MTs applying force to magnetic particles for calibration. A ten second video of the 200nm fSPIONs in the magnetic field of the MTs projected to a 2D image. Note the difference in speed between each frame as the particle gets closer to the MT, which indicates increase in particle velocity. The size variation of the particles is from particles outside the optical section.*

In order to apply MTs for the intracellular AMR, a known force regime must be applied to displace the magnetic particles. According to particle calibration and modulated magnetic field strengths, the forces applied to the particles can vary approximately between 0.1 pN to 500 pN depending on radial distance to MTs (data not shown). This roughly corresponds to a stress on a homogenous network (assumed for model validity) of 0.01 Pa to 100 Pa (based on simple Hertzian contact). As these networks have been shown to stress stiffen under applied strain [12] [14] [43], a low level of stress is required to be in the linear range of elasticity and satisfy the assumptions of the model (see Figure 3). *In vitro* ACTN4: F-Actin networks show an onset of stress stiffening at ~2 Pa, while Myosin/ FLNa/ F-Actin networks show this onset at ~1 Pa [43]. This corresponds to forces on the network of 100 pN or less. As this network are only partially representative of *in*

*vivo* network mechanical properties, the forces required to apply linear elastic strain to the cytoskeleton will vary from these approximations. However, the MTs are built and calibrated to apply forces in these linear ranges for mechanical characterization of the network.

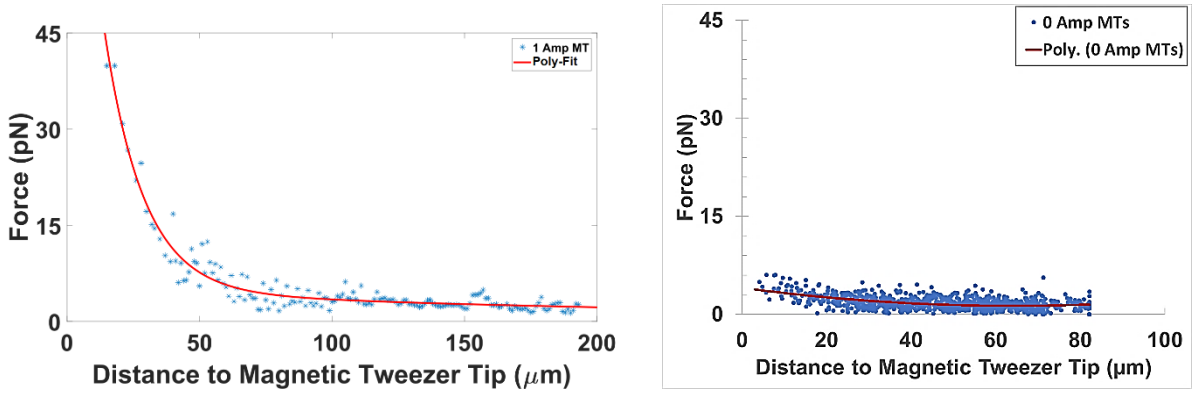


*Figure 15. Force-Distance relation of the MTs with 200nm fSPIONs in glycerol: water colloidal suspension with 1A charged the through inductor (Left) and 0 Amps charged through the inductor (Right). Particles will experience a force regime depending on the radial distance from the MTs tip.*

During regular cycles of on-off, the MTs developed a remnant magnetization in the range of 50 Gauss (see Figure 13-Left) or 3-6 pN of force (see Figure 15-Right). Remnant magnetization is the property of all materials that are influenced by an external magnetic field that is caused by a partial alignment of the magnetic domains within the material and imparts a polarity of charges. As the magnetic field supplied from the inductor is sufficient to impart alignment of the domains within mu-metal, this was expected. However, the unique property of mu-metal is its low remnant magnetization compared to other ferromagnetic materials [41], which is measured to be approximately 10% of the magnetic field strength when the magnetic force is removed. The limited remnant magnetization was expected to provide negligible forces on particles during calibration and experimental force regimes, due to a very small magnetic field gradient Although, the remnant

magnetization was apparent when the MTs were calibrated and it displayed a force regime despite the inductor being uncharged. Several attempts were made to remove the remnant magnetization. This included reversing the DC-source current to the inductor in the 10 – 250 mA range (limit of the power supply), which is within the coercivity levels of the mu-metal for the magnetic field applied. Additionally, a non-polarized electrolytic capacitor was placed in parallel with the inductor as discussed by Sato *et al* [38], which theoretically applies a decaying sinusoidal current that would match the coercivity of the mu-metal to remove the remnant magnetization. One method of removing the remnant magnetization is through heating the mu-metal core to its Curie temperature of 460°C, which would scramble the alignment of the magnetic domains within the material. However, this was not attempted as the permanently attached inductor would have been destroyed. Unfortunately, we were unsuccessful in removing the remnant magnetization of the mu-metal by a sufficient amount to allow the use of the MTs in live cell microrheology. Due to the complications mentioned above, we were unable to apply specific force regimes on particles endocytosed by or attached to cells as they had a remnant magnetic field applying an undesired force. The remnant magnetic force regime applied a prestress to the particles, and thus the cell's cortex. This force could not be accounted for in the equivalent model of cytoplasmic creep compliance, and therefore could not be used to measure creep compliance of the experimental cell lines.

A feasible solution to the remnant magnetization during experiments is through controlled and monitored magnetic field reversals. The coercive force required to remove the remnant magnetization from a saturated mu-metal material is known to be approximately 0.4 A/m [41]. As a result, the calculated opposing magnetizing force

supplied by the inductor should be in the low milliamps range, not currently available with the current sources and inductors available for this study. The magnetizing force required can be achieved through controlled incremental increases in the current supplied to the inductor, while monitoring the magnetic field strength from the MTs using a calibrated hall sensor. The field reversal would require a circuit design that would apply an opposing field from the MTs remnant magnetization. This improvement is currently being implemented by a group of electrical engineering undergraduate students.

Despite not yet being able to apply known and controllable forces on cells in this study, the MTs present an ideal means of elucidating the mechanical properties of the cell with minimal methodological artefacts, as previously shown [8] [27] [29] [33]. The device, with proper calibration and degaussing procedure described above, is capable of applying a modulated force on magnetic particles within a variable distance from the tip. For particles in or on cells, the method can apply a step-stress to quantify the viscous flow of the network and thus its relaxation time.

# 4. Conclusion

The cell is a complex material with rate- and time-dependent mechanical properties, which are highly regulated by a dynamic cytoskeleton. Elucidating these properties at subcellular length scales has been an ongoing challenge for scientists. Instruments and methodologies are constantly being improved or developed in order to understand the fundamental building blocks of life. The study presented here is part of a growing population of research into discovering the physical nature of life.

The physical properties of the cells with endogenously produced crosslinkers with variable binding kinetics have been quantified and qualified by PMR and AMR techniques. Using PMR, the cell is shown to be a weakly elastic solid with viscous dissipation that is decreased as the binding affinity of the ACTN4 crosslinker is increased (ACTN4-K255E). These cells are also shown to transition from solid-like to liquid-like behavior at 2 times slower timescales when comparing ACTN4-K255E to WT ACNT4. Equivalent responses are recovered in both cell lines when subjected to ROCK-pathway inhibitors, suggesting an active contribution to cytoplasmic mechanics. These results are based on fast timescales inherent in PMR, but AMR is further applied to these cells to discover the slower timescales of these binding kinetics.

When using the OMTC AMR technique, the ACTN4-K255E is shown to exhibit slower relaxation times in line with the increase of the binding kinetics of the crosslinker. A 3-fold decrease in relaxation times was observed in ACTN4-K255E crosslinked cells as previously seen *in vitro.* Under the effect of ATP depletion, these cell lines show similar relaxation times suggesting an active role in the relaxation of the network. In all cases, the variability of the relaxation times was considerable due to the nature of model fit

parameters. The normal cell to cell variability was compounded by variability in the model fitting. In order to circumvent the complications of the methodology, a MTs was developed to apply more controlled forces for AMR.

A set of MTs was designed and built in house as a means to control magnetically induced force on magnetic particles with high spatiotemporal accuracy. Magnetophoresis of particles was achieved, which allowed the device to be successfully calibrated. Quantification of the magnetic field strength and force induction on particles revealed a residual magnetization in the device. This caused an low force induction of particles within range of the MTs when no force is expected. Due to the presence of the remnant forcing, step-stress regime could not be applied to cells. Further work is required to achieve a zero-remnant force when the MTs are “off”.

## References


[1] H. Lodish, A. Berk, S. L. Zipursky and a. et, Molecular Cell Biology, New York: W H Freeman, 2000.

[2] K. E. Kasza, A. C. Rowat, J. Liu, T. E. Angelini, C. P. Brangwynne, G. H. Koenderink and D. A. Weitz, "The cell as a material," *Current Opinion in Cell Biology,* vol. 19, pp. 101-107, 2007.

[3] T. G. Mason, K. Ganesan, J. H. van Zanten, D. Wirtz and S. C. Kuo, "Particle Tracking Microrheology of Complex Fluids," *Physical Review Letters,* vol. 79, no. 17, pp. 3282-3285, 1997.

[4] S. Lin, D. Chen, Y. Xie, X. Zhi, Q. Wei, F. Pan and D. Cui, "Single Cell Manipulation Technology," *Nano Biomedical Engineering,* vol. 7, no. 3, pp. 75-91, 2015.

[5] M. Guo, A. J. Ehrlicher, M. H. Jensen, M. Renz, J. R. Moore, R. D. Goldman, J. Lippincott-Schwartz, F. C. Mackintosh and D. A. Weitz, "Probing the Stochastic, Motor-Driven Properties of the Cytoplasm Using Force Spectrum Microscopy," *Cell,* vol. 158, pp. 822-832, 2014.

[6] B. Fabry, G. N. Marksym, S. A. Shore, P. E. Moore, R. A. Panettieri Jr, J. P. Butler and J. J. Fredberg, "Signal Transduction in Smooth Muscle - Selected Contribution: Time course and heterogeneity of contractile responses in cultured human airway smooth muscle cells," *Journal of Applied Physiology,* vol. 91, pp. 986-994, 2001.

[7] A. J. Ehrlicher, R. Krishnan, M. Guo, C. M. Bidan, D. A. Weitz and M. R. Pollak, "Alpha-actinin binding kinetics modulate cellular dynamics and force generation," *PNAS,* vol. 112, no. 21, pp. 6619-6624, 2015.

[8] A. R. Bausch, W. Moeller and E. Sackmann, "Measurement of Local Viscoelasticity and Forces in Living Cells by Magnetic Tweezers," *Biophysical Journal,* vol. 76, pp. 573-579, 1999.

[9] J. Tinevez, N. Perry, J. Schindelin, G. M. Hoopes, G. D. Reynolds, E. Laplantine, S. Y. Bednarek, S. L. Shorte and K. W. Eliceiri, "TrackMate: An open and extensible platform for single-particle tracking," *Methods,* vol. 115, pp. 80-90, 2017.

[10] D. G. Thomas and D. N. Robinson, "The fifth sense: Mechanosensory regulation of alpha-actinin-4 and its relevance for cancer metastasis," *Seminars in Cell and Developmental Biology,* vol. 71, pp. 68-74, 2017.

[11] A. Weins, J. S. Schlondorff, F. Nakamura, B. M. Denker, J. H. Hartwig, T. P. Stossel and M. R. Pollak, "Disease-associated mutant alpha-actinin-4 reveals a mechanism for regulating its F-actin-binding affinity," *Proceedings from the National Academy of Science,* vol. 104, no. 41, pp. 16080-16085, 2007.

[12] M. L. Gardel, J. H. Shin, F. C. MacKintosh, L. Mahadevan, P. Matsudaira and D. A. Weitz, "Elastic Behavior of Cross-Linked and Bundled Actin Networks," *Science,* vol. 304, pp. 1301-1305, 2004.

[13] O. Lieleg, K. M. Schmoller, M. M. A. E. Claessens and A. R. Bausch, "Cytoskeletal Polymer Networks: Viscoelastic Properties are Determined by the Microscopic Interaction Potential of Cross-links," *Biophysical Journal,* vol. 96, pp. 4725-4732, 2009.

[14] N. Y. Yao, D. J. Becker, C. P. Broedersz, M. Depken, F. C. MacKintosh, M. R. Pollak and D. A. Weitz, "Nonlinear Viscoelasticity of Actin Transiently Cross-linked with Mutant α-Actinin-4," *Journal of Molecular Biology,* vol. 411, pp. 1062-1071, 2011.

[15] S. M. V. Ward, A. Weins, M. R. Pollak and D. A. Weitz, "Dynamic Viscoelasticity of Actin Cross-Linked with Wild-Type and Disease-Causing Mutant α-Actinin-4," *Biophysical Journal,* vol. 95, no. 10, pp. 4915-4923, 2008.

[16] C. P. Broedersz, M. Depken, N. Y. Yao, M. R. Pollak, D. A. Weitz and F. C. MacKintosh, "Cross-Link-Governed Dynamics of Biopolymer Networks," *Physical Review Letters,* vol. 105, pp. 1-4, 2010.

[17] J. M. Kaplan, S. H. Kim, K. N. North, H. Rennke, L. A. Correia, H. Q. Ton, B. J. Mathis, J. C. Rodriguez-Perez, P. G. Allen, A. H. Beggs and M. R. Pollak, "Mutations in ACTN4, encoding alpha-actinin-4, cause familial focal segmental glomerulosclerosis," *Nature Genetics,* vol. 24, no. 3, pp. 251-256, 2000.

[18] D. Feng, J. Notbohm, A. Benjamin, S. He, M. Wang, L. H. Ang, M. Bantawa, M. Bouzid, E. Del Gado, R. Krishnan and M. R. Pollak, "Disease-causing mutation in α-actinin-4 promotes podocyte detachment through maladaptation to periodic stretch," *Proceedings from the National Academy of Science,* vol. 115, no. 7, pp. 1517-1522, 2018.

[19] M. L. Gardel, M. T. Valentine and D. A. Weitz, "Microrheology," in *Microscale Diagnostic Techniques*, Springer Verlag, 2005, pp. 1-55.

[20] G. Lenormand, E. Millet, B. Fabry, J. P. Butler and J. J. Fredberg, "Linearity and time-scale invariance of the creep function in living cells," *Journal of the Royal Society Interface,* vol. 1, pp. 91-97, 2004.

[21] A. R. Bausch, F. Ziemann, A. A. Boulbitch, K. Jacobson and E. Sackmann, "Local Measurements of Viscoelastic Parameters of Adherent Cell Surfaces by Magnetic Bead Microrheometry," *Biophysical Journal,* vol. 75, pp. 2038-2049, 1998.

[22] J. J. Heinisch, P. N. Lipke, A. Beaussart, S. K. Chatel, V. Dupres, D. Alsteens and Y. F. Dufrene, "Atomic force microscopy – looking at mechanosensors on the cell surface," *Journal of Cell Science,* vol. 125, no. 18, pp. 4189-4195, 2012.

[23] S. M. Mijailovich, M. Kojic, M. Zivokovic, B. Fabry and J. J. Fredberg, "A finite element model of cell deformation during magnetic bead twisting," *Journal of Applied Physiology,* vol. 93, pp. 1429-1436, 2002.

[24] Y. C. Fung, Biomechanics: Mechanical Properties of Living Tissues, New York: Springer Verlag, 1993.

[25] I. S. Grant and W. R. Phillips, Electromagnetism, Manchester: Wiley & Sons, 2008.

[26] S. S. Shevkoplyas, A. C. Siegel, R. M. Westervelt, M. G. Prentiss and G. M. Whitesides, "The force acting on a superparamagnetic bead due to an applied magnetic," *Lab on a Chip,* vol. 7, pp. 1294-1302, 2007.

[27] L. Chen, V. Maybeck, A. Offenhauser and H. J. Krause, "Characterization of the mechanical properties of HL-1 cardiomyocytes with high throughput magnetic tweezers," *Applied Physics Letters,* vol. 107, 2015.

[28] A. H. de Vries, B. E. Krenn, R. van Driel and J. S. Kanger, "Micro Magnetic Tweezers for Nanomanipulation Inside Live Cells," *Biophysical Journal,* vol. 88, pp. 2137-2144, 2005.

[29] S. Shekhar, A. Cambi, C. G. Figdor, V. Subramaniam and J. S. Kanger, "A Method for Spatially Resolved Local Intracellular Mechanochemical Sensing and Organelle Manipulation," *Biophysical Journal,* pp. 395-404, 2012.

[30] M. T. Valentine, Z. E. Perlman, M. L. Gardel, J. H. Shin, P. Matsudaira, T. J. Mitchison and D. A. Weitz, "Colloid Surface Chemistry Critically Affects Multiple Particle Tracking Measurements of Biomaterials," *Biophysical Journal,* vol. 86, pp. 4004-4014, 2004.

[31] H. F. Yee, A. C. Melton and B. N. Tran, "RhoA/Rho-Associated Kinase Mediates Fibroblast Contractile Force Generation," *Biochemical and Biophysical Research Communications,* vol. 280, pp. 1340-1345, 2001.

[32] R. W. Rees, N. A. Fowell, D. J. Ralph, P. D. Kell, S. Moncada and S. Cellek, "Y-27632, A Rho-Kinase Inhibitor, Inhibits Proliferation and Adrenergic Contraction of Prostatic Smooth Muscle Cells," *Journal of Urology,* vol. 170, pp. 2517-2522, 2003.

[33] J. Schindelin, I. Arganda-Carreras, E. Frise and e. al., "Fiji: an open-source platform for biological-image analysis," *Nature methods,* vol. 9, no. 7, pp. 676-682, 2012.

[34] H. Li, B. Xu, E. H. Zhou, R. Sunyer and Y. Zhang, "Multiscale Measurements of the Mechanical Properties of Collagen Matrix," *ACS Biomaterials Science & Engineerings,* vol. 3, pp. 2815-2824, 2017.

[35] A. Bijamov, F. Shubitidze, P. M. Oliver and D. V. Vezenov, "Quantitative modeling of forces in electromagnetic tweezers," *Journal of Applied Physics,* 2010.

[36] M. Plonus, Applied Electromagnetics, McGraw-Hill, 1978.

[37] S. R. Hoole, Computer-aided analysis and design of electromagnetic devices, Elsevier, 1989.

[38] N. Gal, D. Lechtman-Goldstein and D. Weihs, "Particle tracking in living cells: a review of the mean square displacement method and beyond," *Rheologica Acta,* vol. 52, no. 5, pp. 425-443, 2013.

[39] M. Amano, M. Nakayama and K. Kaibuchi, "Rho-Kinase/ROCK: A Key Regulator of the Cytoskeleton and Cell Polarity," *Cytoskeleton,* vol. 67, pp. 545-554, 2010.

[40] Y. Ueki, N. Sakamoto and M. Sato, "Cyclic Force Applied to FAs Induces Actin Recruitment Depending on the Dynamic Loading Pattern," *The Open Biomedical Engineering Journal,* vol. 4, pp. 129-134, 2010.

[41] S. Mijailovich, M. Kojic, M. Zivkovic, B. Fabry and J. J. Fredberg, "A finite element model of cell deformation during magnetic bead twisting," *Journal of Applied Physiology,* vol. 93, pp. 1429-1436, 2002.

[42] J. Hu, S. Jafari, Y. Han, A. J. Grodzinsky, S. Cai and M. Guo, "Size- and speed-dependent mechanical behavior in living mammalian cytoplasm," *Proceeding from the National Academy of Science,* vol. 114, no. 36, pp. 9529-9534, 2017.

[43] Heanjia Super Metals Co, "MuMetal magnetic shielding alloy for aerospace and telecom," October 2018. [Online]. Available: https://super-metals.com/news/mumetal-alloy-for-magnetic-shielding-devices/. [Accessed 1 October 2018].

[44] J. K. Lim, C. Lanni, E. R. Evarts, F. Lanni, R. D. Tilton and S. A. Majetich, "Magnetophoresis of Nanoparticles," *ACS Nano,* vol. 5, no. 1, pp. 217-226, 2011.

[45] G. H. Koenderink, Z. Dogic, F. Nakamura, P. M. Bendix, F. C. MacKintosh, J. H. Hartwig, T. P. Stossel and D. A. Weitz, "An active biopolymer network controlled by molecular motors," *Proceedings from the National Academy of Science,* vol. 106, no. 36, pp. 15192-15197, 2009.

[46] D. Wirtz, "Particle-Tracking Microrheology of Living Cells: Principles and Applications," *Annual Review of Biophysics,* vol. 38, pp. 301-326, 2009.

[47] J. Xu, D. Wirtz and T. D. Pollard, "Dynamic Cross-linking by a-Actinin Determines the Mechanical Properties of Actin Filament Networks," *Journal of Biological Chemistry,* vol. 273, no. 16, pp. 9570-9576, 1998.

[48] J. K. Liao, M. Seto and K. Noma, "Rho Kinase (ROCK) Inhibitors," *Journal of Cardiovascular Pharmacology,* vol. 50, no. 1, pp. 17-24, 2009.

# Appendix

## Supplemental Figures

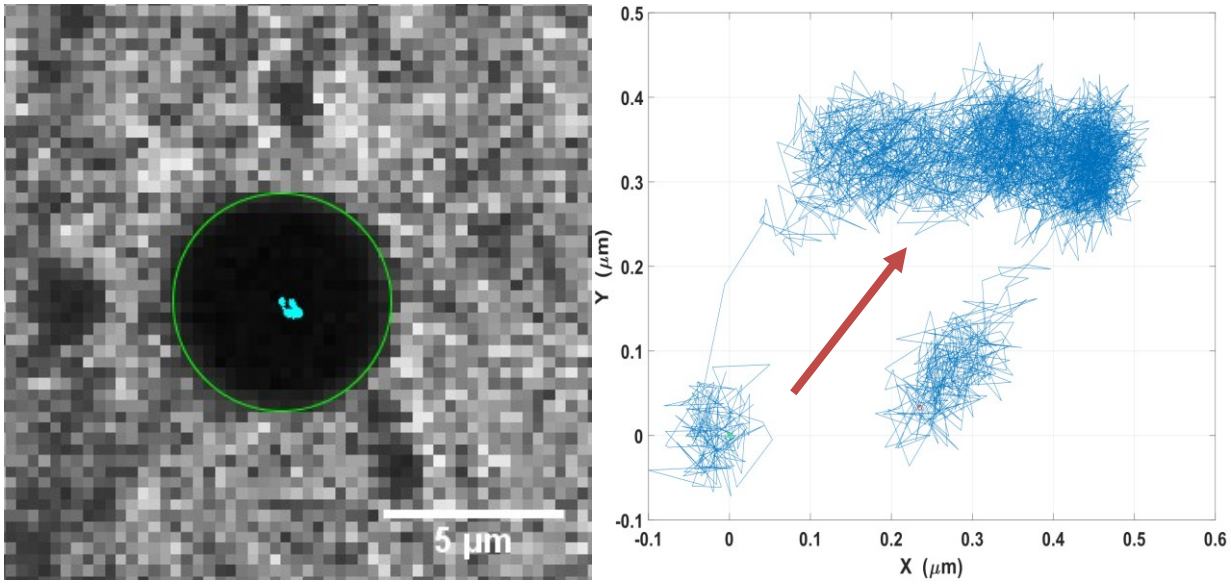


*Figure 16. Non-linear particle displacement under OMTC device forcing regime.* ***Left*** *– Particle tracking of a 4.66 μm ferrimagnetic particle after being displaced for a 2 minute interval. Searching algorithm using circles of specific diameter is displayed (green) for current frame, while the intensity weighted center-of-mass of each frame is shown in center (blue).* ***Right*** *– Large scale displacement map of the tracked positions using tracking algorithm (blue) overlaid with the forcing direction of the OMTC device (red). Non-linear displacement is seen in position data as the particle is displaced from origin (green circle) to end position (red circle).*

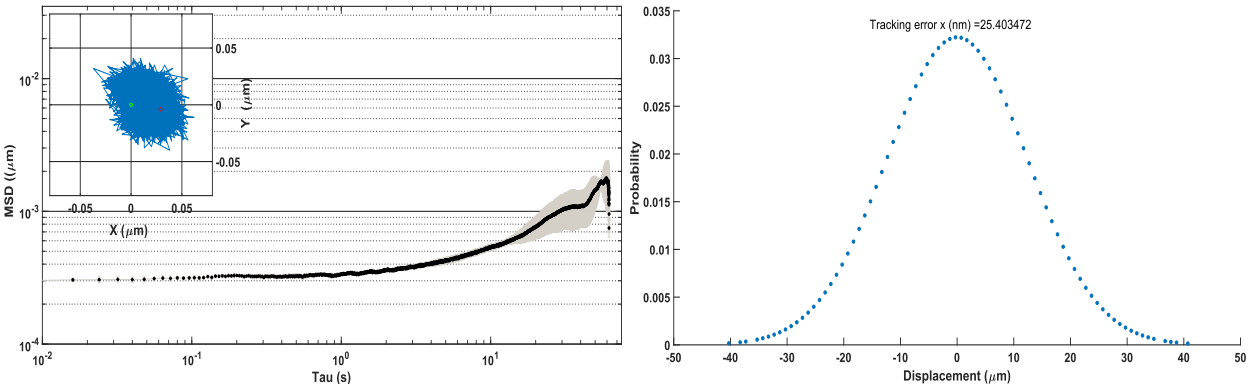


*Figure 17. MSD floor and tracking error.* ***Left –*** *The mean squared displacement of a 4.6 μm particle adhered to the surface of a glass slide and tracked over 1-minute interval on a Leica confocal TCS SP8 microscope at 27 frames/s. The almost constant MSD value indicates the particle is highly constrained in movement due to its adherence to the glass surface. Increase at long time scales (>10s) indicates drift or shifting of the particle in space. This error is likely the same in live cell particle tracking.* ***Inset –*** *tracking of particle with TrackMate.* ***Right –*** *Probability of particle displacement from its initial location, which follows a normal distribution. Tracking Error is the full width at half maximum of this normal distribution (25 nm), which is 10% of the image resolution of 233 nm.*

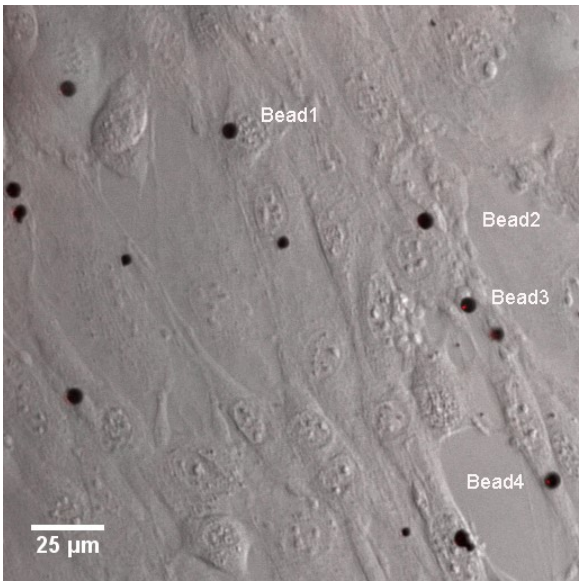


*Figure 18. Culture dish with WT ACTN4 cell line during OMTC creep compliance measurement. Cells are seeded to a high density in order to have a dense collection of cells per frame. This enables high throughput data acquisition for statistical significant results.*

## MatLab Code

### Tracking Error

```
function [tracking_error_r] = trackingError(X,Y,pixelsize)
%% Tracking Error of particles from TrackMate Plugin for ImageJ
% trackingError(X,Y,T,pixelsize): take the X and Y positions of the
% particles and calculates the tracking error. The tracking algorithm
% assumes the particles are stationary over time.
if nargin < 3, pixelsize = 1; end
X=X.*pixelsize*1000;
Y=Y.*pixelsize*1000;
%% X-position calculation
    mu_x=mean(X);  % mean of x-position
    x_upd=X-mu_x;  % x-axis
    x_std=std(X);  % standard deviation of x-position
    x_var=var(X);  % variance in x-position
    p1_x = -.5 * ((X - mu_x)/x_std) .^ 2; % Gaussian fit
    p2_x = (x_std * sqrt(2*pi));
    f_x = exp(p1_x) ./ p2_x;
    tracking_error_x=2*x_std;

tracking_erro_x_final=tracking_error_x;%[tracking_erro_x_final,tracking_error
_x];
    errorx=mean(tracking_erro_x_final);
    figure(1)
    hold on
    plot(x_upd,f_x,'ko','MarkerSize',4);
        xlabel('\mum');ylabel('Probability');
        set(gca,'fontsize',18);
        text(0,max(f_x),sprintf('Tracking error x (nm) =%f',errorx))
%% Y-position calculation (Gaussian fit)
    mu_y=mean(Y);  % mean of y-position
    y_std=std(Y);  % standard deviation of y-position
    y_upd=Y-mu_y;
    y_var=var(Y);   % variance in y-position
    p1_y = -.5 * ((Y - mu_y)/y_std) .^ 2;  % Gaussian fit
    p2_y = (y_std * sqrt(2*pi));    % (sigma*sqrt(2*pi))
    f_y = exp(p1_y) ./ p2_y; % exp(-1/2.^((y-
mu)./(sigma))).//((sigma*sqrt(2*pi)))
    tracking_error_y=2*y_std;

tracking_erro_y_final=tracking_error_y;%[tracking_erro_y_final,tracking_error
_y];
    errory=mean(tracking_erro_y_final);
    figure(1)
    hold on
    plot(y_upd,f_y,'.');
        set(gca,'fontsize',18);
        text(0,max(f_x),sprintf('Tracking error y (\mum) =%f',errory))
%% Gaussian fit of x and y combined
    r=sqrt((X.^2)+(Y.^2));
    mu_r=mean(r);
    r_upd=r-mu_r;
    r_std=std(r);
    p1_r = -.5 * ((r - mu_r)/r_std) .^ 2;  % -1/2.^((y-mu)./(sigma))
    p2_r = (r_std * sqrt(2*pi));    % (sigma*sqrt(2*pi))
    f_r = exp(p1_r) ./ p2_r;
```

```
    tracking_error_r=2*r_std;

tracking_erro_r_final=tracking_error_r;%[tracking_erro_y_final,tracking_error
_y];
    errorr=mean(tracking_erro_r_final);
    figure(1)
    hold on
    plot(r_upd,f_r,'.');
        set(gca,'fontsize',18);
        text(0,max(f_x),sprintf('Tracking error r (nm) =%f',errorr))
end
```

## Optical Magnetic Twisting Cytometry

```
%% Script to run when analysing trajectories from TrackMate
% Takes the xls trajectory files of beads and computes the 1D displacement
% from the 2D coordinates. Assumes that you
warning off
clear variables; close all; clc;
set(0,'DefaultFigureWindowStyle','docked');
matfolder=('C:\Users\csita\Dropbox\Masters_Program\Projects\MatLab_Code');
option = 0; count=0; counter = 0;

while option == 0
    %% Bead Tracks file selection
    [f1, folder1] = uigetfile({'*.xls;*.csv'}, 'Select Magnetic Bead xls or
csv Track file'); %open pop-up to select file
    if ~f1, error('No Track file selected.'); end
    cd(folder1)

    %% Bead Drift file selection
    [f2, folder2] = uigetfile({'*.xls;*.csv'}, 'Select Bead Drift xls or csv
Track file'); %open pop-up to select file
    if f2~=0, driftcor = true; else, driftcor = false; end

    %% Bead Drift file selection
    [f3, folder3] = uigetfile({'*.tif'}, 'Select Bead image file'); %open
pop-up to select file
    if ~f3, alphabeta = false; else, alphabeta = true;  end

    %% Trajectory Calculation
    tracks = sortXLSData([folder1 f1]); %#ok<*SAGROW>
    if driftcor == true
        drifts = sortXLSData([folder2 f2]);
        % dedrifts the tracks using the drift channel tracks
        ddtracks = dedrift(tracks,drifts);
    else
        ddtracks = tracks;
    end

    %% Plot Displacement Curves
    cd(matfolder)
    if alphabeta == true
        [af,~] = alphabetaFactor([folder3 f3],[folder3 f3]);
    else
```

```
        af = 1;
    end
    data1d = position2Dto1D(ddtracks);
    ddtracks(:,[1 2]) = ddtracks(:,[1 2])-ddtracks(1,[1 2]);
    figure(99)
    hold on

plot(ddtracks(:,1)./max(abs(ddtracks(:,1))),ddtracks(:,2)./max(abs(ddtracks(:
,2))),...

ddtracks(1,1),ddtracks(1,2),'og',ddtracks(end,1)./max(abs(ddtracks(:,1))),...
        ddtracks(end,2)./max(abs(ddtracks(:,2))),'or')
    figure(100)
    subplot(2,1,1)
    hold on
    yyaxis right
    plot(data1d(:,1),data1d(:,3),'--') % T vs Force
    xlim([min(data1d(:,1)) max(data1d(:,1))])
    ylabel('Torque (pNnm)','FontSize',16,'FontWeight','bold')
    yyaxis left
    plot(data1d(:,1),data1d(:,2),':') % T vs J
    ylabel('Specific Creep Compliance (\mumPa^-
^1)','FontSize',16,'FontWeight','bold')
    subplot(2,1,2)
    hold on
    yyaxis right
    plot(data1d(:,1),data1d(:,3),'--') % T vs Force
    xlabel('Time (sec)','FontSize',16,'FontWeight','bold')
    xlim([min(data1d(:,1)) max(data1d(:,1))])
    ylabel('Torque (pNnm)','FontSize',16,'FontWeight','bold')
    yyaxis left
    plot(data1d(:,1),data1d(:,2)*af,':') % T vs J
    ylabel('Creep Compliance (\mumPa^-^1)','FontSize',16,'FontWeight','bold')

    %% Plot MSD Curves
    cd(matfolder)
    [msd,~] = msdBeads(ddtracks(:,1:3));
    trackingerror = trackingError(ddtracks(:,1),ddtracks(:,2)) %#ok<NOPTS>
    cd(folder1)

    %% Curve Fitting
    t1s = (1/mean(diff(data1d(:,1)))); %finds number of frames in 1s
    dt = mean(diff(data1d(:,1)));
    [row,~]=find(data1d(:,3)~=0); row = row-3;
    % Curve fit based off of Bausch 1999 model of cell surface.
    % J(t) = (1/a)*(1-(b/(a+b))*exp(-x*(a*b)/(d*(a+b))))+x/c
    cftool(0:dt:(length(row)-1)*dt,data1d(row,2));

% %     % MT Jump
% %     cftool(data1d(row(1):row(2*t1s),1),data1d(row(1):row(2*t1s),2));
% %
% %     %Plateau
% %     cftool(data1d(row(t2s):row(end),1),data1d(row(t2s):row(end),2));
%     f = findall(0,'Type','Figure');
%     waitfor(f(1))
```

```
    %% Add more overlays of plotted velocity/forces
    counter=counter+1;
    choice = questdlg('Would you like to continue?', ...
        'Additional Experimental Runs', ...
        'Yes','No','Yes');
    switch choice
        case 'Yes'
            option = 0;
        case 'No'
            option = 1;
    end
    ft{counter} = data1d; tt{counter} = ddtracks; %#ok<*AGROW>

    clear f1 pathname1 f2 f3 f4 tipx tipy ddtracks ftracks tracks drifts
verttracks
end

cd(folder1)
save('data-compiled.mat','ft','tt')

%%=========================================================================
function dataxytd = sortXLSData(data)
%% Sort tracking information from TrackMate xls file
%  DATAXYT = SORTXLSDATA(data) Takes user passed data from trackMate in order
to
%  parse data into different cells. Each cell is the X,Y,T data of a
%  particular bead track.
%  - (data) is a large assorment of values determined during TrackMate
%  analysis in xls format. More components can be added to the output cell
%  array as desired for downstream Track analysis.
%  - dataxytvdp is a cell array of different bead tracks with x in the
%  first column, y in the second column, t in the third column, frame# in
%  the fourth column, vx in the 5th column, vy in the 6th column, V in the
%  7th column, dx in the 8th column, dy in the 9th column, D in the 10th
%  column.
if isempty(data), errordlg('Data not found'), return, end
if strcmp(data(end-2:end),'xls')
    [data1,~] = xlsread(data);
elseif strcmp(data(end-2:end),'csv')
    data1 = csvread(data,1,1);
end
if size(data1,2)~=22, dc = 2; else, dc = 0; end

t = data1(:,9-dc);  %T-pos data from column#9(7) in TrackMate XLS(CSV)
x = data1(:,6-dc);  %X-pos data from column#6(4) in TrackMate XLS(CSV)
y = data1(:,7-dc);  %Y-pos data from column#7(5) in TrackMate XLS(CSV)
frame = data1(:,10-dc);
dataxytd = [x,y,t,frame];    % Again add additional Track components in this
matrix
dataxytd = getDisp(dataxytd);
end

%%=========================================================================
function dataxytd = getDisp(dataxyt)
%% Instantaneous Velocity from position and time data
%  GETDISPVEL(data) Takes x and y coordinates and time data in the form of
```

```
%  cell array with each cell being a bead track.
%  - (data) should be a cell array of different bead tracks with x in the
%  first column, y in the second column, t in the third column, and frame#
%  in 4th column.
%  - returns a displacement and velocity matrix with x and y components of
%  displacement and velocity as well as their magnitudes.
[~,n]=size(dataxyt);
if isempty(dataxyt)
    error('Data not found')
elseif n<3
    error('Data is not in format of x(:,1), y(:,2), and t(:,3)')
end
dx = gradient(dataxyt(:,1));  % X component of displacement
dy = gradient(dataxyt(:,2));  % Y component of displacement
d = sqrt((dx.^2)+(dy.^2));          % Scalar of displacement
displacement = [dx,dy,d];     % array with all displacements from tracks
dataxytd = horzcat(dataxyt,displacement);
end

%%=========================================================================
function ddtrack = dedrift(beadtrack,beaddrift)%,img)
%% Remove drift channel from primary track
% dedrift(tracks,drift) removes the drift from tracks by taking the
% displacment of the drift and removes it from the tracks of the beads in
% the MT trap. To avoid compounding error, the trend of the drift is
% removed from x and y displacements over time.
%INPUT:
%  - tracks is a matrix of bead positions with x in the first column, y
%  in the second column, t in the third column, frame# in the fourth
%  column, dx in the 5th column, dy in the 6th column, D in the 7th column.
%  - drift is a matrix of bead positions with x in the first column, y in
%  the second column, t in the third column, frame# in the fourth column,
%  dx in the 5th column, dy in the 6th column, D in the 7th column. Drift
%  is assumed to be unmoving feature from image sequence.
%OUTPUT:
%  - ddtracks is the matrix of points of the bead track with the drift of
%  the particles removed.

mn = 1:2; % mn = x or y column of each cell
t = beadtrack(:,3);
if length(beadtrack)~=length(beaddrift)
    xint =
interp1(beaddrift(:,3),beaddrift(:,1),min(t):mean(diff(t)):max(t));
    yint =
interp1(beaddrift(:,3),beaddrift(:,2),min(t):mean(diff(t)):max(t));
else
    xint = beaddrift(:,1);
    yint = beaddrift(:,2);
end
% Find non-linear trend in Drift data
f = fit(t,yint,'poly3'); % t vs y-direction
fy = feval(f,t);
f = fit(t,xint,'poly3'); % t vs x-direction
fx = feval(f,t);
fxy = [0 0;cumsum(diff([fx-fx(1) fy-fy(1)]))];
```

```
% Removes Drift from original positions
beadtrack(:,mn) = beadtrack(:,mn)-fxy;

% Correct Displacement
beadtrack(:,mn+4) = [0 0;diff(beadtrack(:,mn))];
beadtrack(:,7) = sqrt(beadtrack(:,5).^2+beadtrack(:,6).^2);
ddtrack = beadtrack;
end

%%=========================================================================
function [data1d,h] = position2Dto1D(data2d)
%% Manipulate Bead track from 2D to 1D for Active MicroRheology
% Take magnetic bead tracking data from TrackMate and reduces the
dimensionality to 1D.
% input:
%   - data2d should be the tracked coordinates of the beads according to
%   trackMate datasets
% Output:
%   - data1d is a 1-Dimensional dataset of t (:,1), radial distance from
%   origin (:,2), and assumed Force regime (:,3)

%% Checks to see data is present and assigns to temp variables
if isempty(data2d), error('No data to process'), end
t=data2d(:,3); x=data2d(:,1); y=data2d(:,2); force = zeros(length(t),1);
data1d=zeros(length(t),3);

%% Finds where the most amount of displacement has occured before and after
% OMTC is turned on and again turned off.
t1s = 1/mean(diff(t)); % #frames in 1sec
d = sqrt((x-x(1)).^2+(y-y(1)).^2);
dg = gradient(smoothdata(d,'movmedian'));
[~,ind1]= max(dg(1:length(t)/2));
if ind1<t1s, ind1 = t1s+1; end
[~,ind2] = max(abs(dg(ind1*1.5:end)));
    ind2 = ind2+ind1*1.5-5*t1s;
if ind2>length(t), ind2 = ind2-(length(t)-ind2(end)); end
if isempty(ind1)||isempty(ind2)||ind2<ind1
    figure(1000)
    set(gcf,'units','normalized','outerposition',[0 0 1 1])
    plot(t,dg)
    grid on; grid minor;
    answer = inputdlg({'Enter time to MT turned on (s):','Enter time to MT
turned off (s):'},...
        'Input',[1 35],{'5','120'});
    close(1000)
    ind1 = str2double(answer{1})*t1s;
    ind2 = str2double(answer{2})*t1s;
end

%% Sets beginning of tracks to center at [0,0]
meanx1 = mean(x(1:ind1-t1s)); meany1 = mean(y(1:ind1-t1s));
x = x - meanx1; y = y - meany1;
d = sqrt(x.^2+y.^2);

%% Find intersection of rise and plateau lines to give height of rise
%First line is found from 1/10sec before and 1/2sec after the rise index
```

```
l1 = fit(t(floor(ind1-t1s/10):floor(ind1+t1s/2)),d(floor(ind1-
t1s/10):floor(ind1+t1s/2)),'poly1');
%Second line is found from 10sec after the rise index until the halfway mark
l2 = fit(t(ind1+10*t1s:length(t)/2),d(ind1+10*t1s:length(t)/2),'poly1');
h = l1.p1*((l2.p2-l1.p2)/(l1.p1-l2.p1))+l1.p2;
t60 = ind1+60*t1s; t120 = ind1+120*t1s;
Rr60 = (mean(d(t60-5:t60+5)))/h;
Rr120 = (mean(d(t120-5:t120+5)))/h;
disp(['Rise Height is ',num2str(h),181,'m'])
disp(['Rise Ratio at 60s is ',num2str(Rr60)])
disp(['Rise Ratio at 120s is ',num2str(Rr120)])

%% Flips coordinates to 1st quadrant of 2D cartesian plane
if sum(sign(x))<0, x = x.*-1; end
if sum(sign(y))<0, y = y.*-1; end

%% Calculate distance from (0,0)
r = sqrt(x.^2+y.^2);  % Radius of displacement from Origin

%% Force regime T(t) = C_bead*C_coil_I(t) from Mijailovich 2002
force(ind1:ind2,1) = 2.08*35.3*1;

%% Creep Compliance Calculation according to Bausch 1999
gf = 6*pi()*4.66/2; % Geometric factor of OMTC beads
J = r./force.*gf;
J(isinf(J))=0;

data1d(:,1) = t;     % Time
data1d(:,2) = J;     % Creep Compliance
data1d(:,3) = force; % Force regime
end
```

## Magnetic Tweezers

```
%% MTForcePlotter Calculates and plots the force and Velocity of tracked
tracer particles
%Input:
% - The script can take the tif files of the 'drift' and track from the user
and
% calculates the Force and velocity from the associated xls or mat files
% outputed from TrackMate or FIESTA, respectfully. The user is also
% prompted to input the size of the tracer particles as well as the
% viscosity of the medium.
%Output:
% - The script will save the uncorrected and corrected tracer particle
% tracks using the name of the tif file of magnetic particles as template
% and appending 'data-' at the beginning in the current folder (Example:
% 'data-1A-glycerol65-20170809.mat').
warning off
clear variables; close all; clc;
set(0,'DefaultFigureWindowStyle','docked');
matfolder=('C:\Users\Chris\Dropbox\Masters_Program\Projects\MatLab_Code\');
option = 0; count=0; counter = 0;
```

```
while option == 0
    %% Bead Tracks file selection
    [f1, folder1] = uigetfile({'*.xls;*.csv'}, 'Select Magnetic Bead xls or
csv Track file'); %open pop-up to select file
    if ~f1, error('No Track file selected.'); end
    cd(folder1)

    %% Bead Drift file selection
    [f2, folder2] = uigetfile({'*.xls;*.csv'}, 'Select Bead Drift xls or csv
Track file'); %open pop-up to select file
    if f2~=0, driftcor = true; else, driftcor = false; end

    %% Bead Drift file selection
    [f3, folder3] = uigetfile({'*.tif'}, 'Select Bead image file'); %open
pop-up to select file
    if ~f1, error('No Track file selected.'); end

    %% Trajectory Calculation
    tracks = sortXLSData([folder1 f1]); %#ok<*SAGROW>
    if driftcor == true
        drifts = sortXLSData([folder2 f2]);
        % dedrifts the tracks using the drift channel tracks
        ddtracks = dedrift(tracks,drifts);
    else
        ddtracks = tracks;
    end
    prompt = {'Enter viscosity in Pa*s: ','Enter Radius of Particles
(nm)','Distance to Tip (\mum):'};
            dlg_title = 'Parameters';
            num_lines = 1;
            defaultans = {'0.1','0.1','1000'};
            answer = inputdlg(prompt,dlg_title,num_lines,defaultans);
    viscosity = str2double(answer{1}); % Viscosity of fluid in Pa*s
    radius = str2double(answer{2}); % Radius of the particles
    stokesconst = 6*pi()*viscosity*radius; %scalar to translate velocity to
force
    [picszy,picszx] = size(imread([folder3 f3]));
    distance = str2double(answer{3}).*-1-picszx/2;
    %% Plot Force Curves
    for i = 1:length(ddtracks)
        velocity{i} = ddtracks{i}(:,9);
        distTotip{i} = getTipDistance(ddtracks{i},distance*ones(picszy-
1,1),1:picszy-1);
        force{i} = velocity{i}.*(stokesconst);% Force Calculation using
Stokes Law: F = 6*pi*viscosity*radius*velocity
    %% Plot Velocity Curves
        figure(99)
        hold on
        title(['Velocity of ',num2str(radius*2000),'nm SPIONs-Compiled']);
        plot(distTotip{i}',velocity{i},'*b');
        xlabel('Distance to Tip (um)');
        ylabel('Velocity (um/s)');
        %,['Fit: ',num2str(fit1.p1),'x^2 + ',num2str(fit1.p2),'x +
',num2str(fit1.p3)])
    %% Plot Force Curves
        figure(100)
```

```
        hold on
        title(['Force of ',num2str(radius*2000),'nm SPIONs-Compiled']);
        plot(distTotip{i},force{i},'*r')
        xlabel('Distance to Tip (um)');
        ylabel('Force (pN)');
        %,['Fit: ',num2str(fit2.p1),'x^2 + ',num2str(fit2.p2),'x +
',num2str(fit2.p3)])
    %% Plot X-Y movement
        figure(101)
        hold on
        title(['XY-movement of ',num2str(radius*2000),'nm SPIONs-Compiled']);
        plot(ddtracks{i}(:,1),ddtracks{i}(:,2),'.');
        xlabel('x (\mum)');
        ylabel('y (\mum)');
        if i == 1
            dista = distTotip{i}';
            forc = force{i};
        else
            dista = [dista;distTotip{i}']; %#ok<*AGROW>
            forc = [forc;force{i}];
        end
    end
    [sortdist,indx] = sort(dista);
    sortforc = forc(indx);
    figure(100)
        hold on
        title(['Force of ',num2str(radius*2000),'nm SPIONs-Compiled']);
        fit1 = fit(sortdist,sortforc,'poly1');
        plot(fit1,sortdist,sortforc,'*r')
        xlabel('Distance to Tip (um)');
        ylabel('Force (pN)');
%% Add more overlays of plotted velocity/forces
    counter=counter+1;
    choice = questdlg('Would you like to continue?', ...
            'Additional Experimental Runs', ...
            'Yes','No','Yes');
    switch choice
        case 'Yes'
            option = 0;
        case 'No'
            option = 1;
    end
    datastr = ['data-',f1(1:end-4),'.mat'];
    if counter == 1
        ddt = ddtracks; tt = tracks;
    else
        ddt = horzcat(ddt,ddtracks); tt = horzcat(tt,tracks);
    end
    clear f1 pathname1 f2 f3 f4 tipx tipy ddtracks ftracks tracks drifts
verttracks
    clear disTotip velocity force
    clear f1 pathname1 f2 f3 f4 tipx tipy ddtracks ftracks tracks drifts
verttracks
end

cd(folder1)
save('data-compiled.mat','ddt','tt')
```

```
%%=============================================================================
function dataxytvdp = sortXLSData(data)
%% Sort tracking information from TrackMate xls file
%  DATAXYT = SORTXLSDATA(data) Takes user passed data from trackMate in order
to
%  parse data into different cells. Each cell is the X,Y,T data of a
%  particular bead track.
%  - (data) is a large assorment of values determined during TrackMate
%  analysis in xls format. More components can be added to the output cell
%  array as desired for downstream Track analysis.
%  - dataxytvdp is a cell array of different bead tracks with x in the
%  first column, y in the second column, t in the third column, frame# in
%  the fourth column, vx in the 5th column, vy in the 6th column, V in the
%  7th column, dx in the 8th column, dy in the 9th column, D in the 10th
%  column.
count = 1;
if isempty(data), errordlg('Data not found'), return, end
if strcmp(data(end-2:end),'xls')
    [data,~] = xlsread(data);
elseif strcmp(data(end-2:end),'csv')
    data = csvread(data,1,1);
end
if size(data,2)~=22, dc = 2; else, dc = 0; end
for i = 1:data(end,2)
    [temp,~] = find(data(:,2)==i);
    if ~isempty(temp)
       dataxyt{count}=[data(temp,6-dc),data(temp,7-dc),data(temp,9-dc)];
       count=count+1;
    end
    clear temp
end
dataxytvdp = getDispVel(dataxyt);
end

%%=============================================================================
function dataxytdv = getDispVel(dataxyt)
%% Instantaneous Velocity from position and time data
%  GETDISPVEL(data) Takes x and y coordinates and time data in the form of
%  cell array with each cell being a bead track.
%  - (data) should be a cell array of different bead tracks with x in the
%  first column, y in the second column, t in the third column, and frame#
%  in 4th column.
%  - returns a displacement and velocity matrix with x and y components of
%  displacement and velocity as well as their magnitudes.
[~,n]=size(dataxyt);
if isempty(dataxyt)
    error('Data not found')
end
for i = 1:n
        dt = mean(diff(dataxyt{i}(:,3)));
        dx = [0;diff(dataxyt{i}(:,1))];  % X component of displacement
        dy = [0;diff(dataxyt{i}(:,2))];  % Y component of displacement
        d = sqrt((dx.^2)+(dy.^2));          % Scalar of displacement
        displacement = [dx,dy,d];     % array with all displacements from
tracks
```

```
        vx = [0;diff(dataxyt{i}(:,1))./dt];  % X component of velocity
        vy = [0;diff(dataxyt{i}(:,2))./dt];  % Y component of velocity
        v = sqrt((vx.^2)+(vy.^2));          % Scalar of velocity
        velocity = [vx,vy,v];     % array with all displacements from tracks
        dataxytdv{i} = horzcat(dataxyt{i},displacement,velocity);
end
end

%%=========================================================================
function ddtrack = dedrift(beadtrack,beaddrift)%,img)
% dedrift(tracks,drift) removes the drift from tracks by taking the
% displacment of the drift and removes it from the tracks of the beads in
% the MT trap. To avoid compounding error, the trend of the drift is
% removed from x and y displacements over time.
%INPUT:
%  - tracks is a matrix of bead positions with x in the first column, y
%  in the second column, t in the third column, frame# in the fourth
%  column, dx in the 5th column, dy in the 6th column, D in the 7th column.
%  - drift is a matrix of bead positions with x in the first column, y in
%  the second column, t in the third column, frame# in the fourth column,
%  dx in the 5th column, dy in the 6th column, D in the 7th column. Drift
%  is assumed to be unmoving feature from image sequence.
%OUTPUT:
%  - ddtracks is the matrix of points of the bead track with the drift of
%  the particles removed.

mn = 1:2; % mn = x or y column of each cell
t = beadtrack(:,3);
if length(beadtrack)~=length(beaddrift)
    xint =
interp1(beaddrift(:,3),beaddrift(:,1),min(t):mean(diff(t)):max(t));
    yint =
interp1(beaddrift(:,3),beaddrift(:,2),min(t):mean(diff(t)):max(t));
else
    xint = beaddrift(:,1);
    yint = beaddrift(:,2);
end
% Find non-linear trend in Drift data
f = fit(t,yint,'poly3'); % t vs y-direction
fy = feval(f,t);
f = fit(t,xint,'poly3'); % t vs x-direction
fx = feval(f,t);
fxy = [0 0;cumsum(diff([fx-fx(1) fy-fy(1)]))];

% Removes Drift from original positions
beadtrack(:,mn) = beadtrack(:,mn)-fxy;

% Correct Displacement
beadtrack(:,mn+4) = [0 0;diff(beadtrack(:,mn))];
beadtrack(:,7) = sqrt(beadtrack(:,5).^2+beadtrack(:,6).^2);
ddtrack = beadtrack;
end

%%=========================================================================
function dispxy = getTipDistance(dataxytvd,tipx,tipy)
% GETTIPDISTANCE calculates the distances from specified tip points to the
```

```
% coordinates of the beads.
%INPUT:
% dataxytvd - cell array with each cell being a track and the matrix of
% points being the x, y, t, velocity and displacement vectors of each point
% on the track.
% tipx & tipy - are vectors of x and y coordinates of each point in the MT
% Tip as found by tipMask(image) function.
%OUTPUT:
% dataxytvdp - is the original cell array of tracks with an added vector of
% distances appended to the end of each track from a point on the Tip of MT
for j=1:length(dataxytvd(:,1))
    xyzpoints = [tipx,tipy',zeros(length(tipx),1)];  % Cloud of points
[x,y,z]
    pCloud = pointCloud(xyzpoints);   % PointCloud object for tip
    indpoint = [dataxytvd(j,1),dataxytvd(j,2),0];% point index [xi, yi, zi]
    [~,dists] = findNearestNeighbors(pCloud,indpoint,1);% Matlab function to
find distances of each bead to points of MT tip
    dispxy(j) = dists;  % % Distance is eucladian distance from pointCloud
%         if j>1
%             if dispxy(j)>dispxy(j-1)
%                 dispxy(j)= dispxy(j-1)+dataxytvd{i}(j,11);
%             end
%         end
%         x = abs(tipx-dataxytvd{i}(j,1));        % Compares the distance
from point to all of points in tip
%         y = abs(tipy-dataxytvd{i}(j,2));        % First in x and then in y
%         xy = sqrt(x.^2+y.^2);                   % Checks distances
%         [~, index] = min(xy);                   % Is the index of minimum
of distance
%             dispx(j) = min(x(index));
%             dispy(j) = min(y(index));
%             dispxy(j) = min(xy(index));
%        clear x y xy index
end
end
```

n